**TECHNISCHE UNIVERSITÄT MÜNCHEN**

**Fakultät für Medizin**

**Institut für diagnostische und interventionelle Radiologie**

# Quantification of Proton Density Fat Fraction and Fatty Acid Composition of Triglycerides in Musculoskeletal Tissues using Magnetic Resonance Imaging and Spectroscopy

Stefan Albert Ruschke

Vollständiger Abdruck der von der Fakultät für Medizin der Technischen Universität München zur Erlangung des akademischen Grades eines

Doktor der Naturwissenschaften (Dr. rer. nat.)

genehmigten Dissertation.

| | | |
|---|---|---|
| Vorsitzende: | | Prof. Dr. Gabriele Multhoff |
| Prüfer der Dissertation: | 1. | Priv.-Doz. Dimitrios C. Karampinos, Ph.D. |
| | 2. | Prof. Dr. Axel Haase |
| | 3. | Priv.-Doz. Dr. Marion I. Menzel |

Die Dissertation wurde am 15.11.2017 bei der Technischen Universität München eingereicht und durch die Fakultät für Medizin am 01.08.2018 angenommen.

# Abstract

The musculoskeletal system comprises muscles, bones, cartilage, tendons, ligaments, joints and connective tissue. Many mechanisms in musculoskeletal diseases including osteoporosis or muscle fat infiltration are still not entirely understood and therefore the diagnostic sensitivity may be insufficient. A better understanding of the role of triglycerides in musculoskeletal diseases may be beneficial in order to allow their early diagnosis. The development of triglyceride centered biomarkers which can be non-invasively probed using magnetic resonance (MR) may allow to overcome current challenges of an early diagnosis or characterization in musculoskeletal diseases and may also allow to get a deeper understanding of the underlying mechanisms.

Magnetic resonance imaging (MRI) is a valuable diagnostic tool and known for its high soft tissue contrast. MR allows to differentiate signals based on their chemical shift arising from protons in water molecules and from protons in triglycerides. Two main families of techniques exist to encode chemical shift information in clinical MR: On one hand MR spectroscopy (MRS) focuses on the extraction of chemical shift information and has only very limited spatial information. On the other hand, chemical shift encoding-based imaging aims at retrieving spatial information with very limited information in the chemical shift dimension.

The present cumulative thesis bundles three journal publications in the field of musculoskeletal MR aiming for a) addressing confounding factors in the quantitative measurement of the degree of (un)saturation in triglycerides using MRS, b) the quantitative assessment of proton density fat fraction (PDFF) using chemical shift encoding-based MRI and c) the application of quantitative chemical shift encoding-based water–fat imaging to measure vertebral bone marrow PDFF in pediatrics.

In the first journal publication, a method is described to measure the degree of triglyceride (un)saturation in muscle tissue using MRS. A diffusion-weighted stimulated echo acquisition mode (DW-STEAM) MRS sequence was employed in order to suppress the strong confounding water signal based on differences in the diffusivity between water and triglycerides. The optimized DW-STEAM sequence showed a superior signal-to-noise performance compared to previously applied long echo time point-resolved spectroscopy techniques and can also be used in other tissues with low PDFF to characterize triglyceride (un)saturation.

The second publication describes a phase correction scheme to eliminate confounding factors in time interleaved multi-echo gradient-echo-based quantitative water–fat imaging. The proposed phase correction scheme was found to give accurate and robust complex-based PDFF measurements independent of the chosen resolution and field-of-view size.

Finally, the third journal publication presents how the technique reported in the second journal publication was applied to measure and explore cross-sectional changes with age and intra-individual variations in the vertebral bone marrow PDFF in pediatrics. The measured PDFF showed a sex-independent cross-sectional increase correlating with the natural logarithm of age and an intra-individual decrease from the lumbar to the cervical region.

All developed techniques were and are being used in ongoing clinical studies and research investigations including the fields of osteoporosis, orthopedics and metabolic studies.

# List of Included Journal Publications

The present dissertation is based on the following three journal publications:

JP-I **S. Ruschke**, H. Kienberger, T. Baum, H. Kooijman, M. Settles, A. Haase, M. Rychlik, E. J. Rummeny, and D. C. Karampinos, *"Diffusion-weighted stimulated echo acquisition mode (DW-STEAM) MR spectroscopy to measure fat unsaturation in regions with low proton-density fat fraction"*, Magn Reson Med, vol. 75, no. 1, pp. 32–41, Jan. 2016. DOI: 10.1002/mrm.25578

JP-II **S. Ruschke**, H. Eggers, H. Kooijman, M. N. Diefenbach, T. Baum, A. Haase, E. J. Rummeny, H. H. Hu, and D. C. Karampinos, *"Correction of phase errors in quantitative water–fat imaging using a monopolar time-interleaved multi-echo gradient echo sequence"*, Magn Reson Med, vol. 78, no. 3, pp. 984–996, Sep. 2017. DOI: 10.1002/mrm.26485.

JP-III **S. Ruschke**, A. Pokorney, T. Baum, H. Eggers, J. H. Miller, H. H. Hu, and D. C. Karampinos, *"Measurement of vertebral bone marrow proton density fat fraction in children using quantitative water–fat MRI"*, Magn Reson Mater Phys Biol Med, vol. 30, no. 5, pp. 449–460, Apr. 2017. DOI: 10.1007/s10334-017-0617-0.

The above three journal publications are referred to as JP-I, JP-II and JP-III, respectively. Please refer to Chapter 7 for publication abstracts.

# List of Related Publications

The author contributed also to the following subject-related journal publications (ordered by year of appearance):

J1 D. C. Karampinos, **S. Ruschke**, M. Dieckmeyer, M. Diefenbach, D. Franz, A. S. Gersing, R. Krug, and T. Baum, *"Quantitative MRI and spectroscopy of bone marrow,"* J Magn Reson Imaging, vol. 47, no. 2, pp. 332–353, Feb. 2018.

J2 D. C. Karampinos, C. Holwein, S. Buchmann, T. Baum, **S. Ruschke**, A. S. Gersing, R. Sutter, A. B. Imhoff, E. J. Rummeny, and P. M. Jungmann, *"Proton Density Fat-Fraction of Rotator Cuff Muscles Is Associated With Isometric Strength 10 Years After Rotator Cuff Repair: A Quantitative Magnetic Resonance Imaging Study of the Shoulder,"* Am J Sports Med, vol. 45, no. 9, pp. 1990–1999, Jul. 2017.

J3 M. Dieckmeyer, **S. Ruschke**, H. Eggers, H. Kooijman, E. J. Rummeny, J. S. Kirschke, T. Baum, and D. C. Karampinos, *"ADC Quantification of the Vertebral Bone Marrow Water Component: Removing the Confounding Effect of Residual Fat.,"* Magn Reson Med, vol. 78, no. 4, pp. 1432–1441, Oct. 2017.

J4 C. Cordes, T. Baum, M. Dieckmeyer, **S. Ruschke**, M. N. Diefenbach, H. Hauner, J. S. Kirschke, and D. C. Karampinos, *"MR-Based Assessment of Bone Marrow Fat in Osteoporosis, Diabetes, and Obesity.,"* Front Endocrinol, vol. 7, no. 6, p. 74, 2016.

J5 T. Baum, S. Inhuber, M. Dieckmeyer, C. Cordes, **S. Ruschke**, E. Klupp, P. M. Jungmann, R. Farlock, H. Eggers, H. Kooijman, E. J. Rummeny, A. Schwirtz, J. S. Kirschke, and D. C. Karampinos, *"Association of Quadriceps Muscle Fat With Isometric Strength Measurements in Healthy Males Using Chemical Shift Encoding-Based Water-Fat Magnetic Resonance Imaging.,"* J Comput Assist Tomogr, vol. 40, no. 3, pp. 447–451, May 2016.

J6 T. Baum, C. Cordes, M. Dieckmeyer, **S. Ruschke**, D. Franz, H. Hauner, J. S. Kirschke, and D. C. Karampinos, *"MR-based assessment of body fat distribution and characteristics.,"* Eur J Radiol, vol. 85, no. 8, pp. 1512–1518, Aug. 2016.

J7 D. C. Karampinos, **S. Ruschke**, M. Dieckmeyer, H. Eggers, H. Kooijman, E. J. Rummeny, J. S. Bauer, and T. Baum, *"Modeling of T2* decay in vertebral bone marrow fat quantification,"* NMR Biomed, vol. 28, no. 11, pp. 1535–1542, 2015.

J8 M. Dieckmeyer, **S. Ruschke**, C. Cordes, S. P. Yap, H. Kooijman, H. Hauner, E. J. Rummeny, J. S. Bauer, T. Baum, and D. C. Karampinos, *"The need for T2 correction on MRS-based vertebral bone marrow fat quantification: implications for bone marrow fat fraction age dependence,"* NMR Biomed, vol. 28, no. 4, pp. 432–439, Apr. 2015.

J9 D. C. Karampinos, **S. Ruschke**, O. Gordijenko, E. Grande Garcia, H. Kooijman, R. Burgkart, E. J. Rummeny, J. S. Bauer, and T. Baum, *"Association of MRS-Based*

*Vertebral Bone Marrow Fat Fraction with Bone Strength in a Human In Vitro Model,"* J Osteoporos, vol. 2015, no. 6, pp. 1–8, Apr. 2015.

J10 C. Cordes, M. Dieckmeyer, B. Ott, J. Shen, **S. Ruschke**, M. Settles, C. Eichhorn, J. S. Bauer, H. Kooijman, E. J. Rummeny, T. Skurk, T. Baum, H. Hauner, and D. C. Karampinos, *"MR-detected changes in liver fat, abdominal fat, and vertebral bone marrow fat after a four-week calorie restriction in obese women,"* J Magn Reson Imaging, vol. 42, no. 5, pp. 1272–1280, 2015.

J11 T. Baum, S. P. Yap, M. Dieckmeyer, **S. Ruschke**, H. Eggers, H. Kooijman, E. J. Rummeny, J. S. Bauer, and D. C. Karampinos, *"Assessment of whole spine vertebral bone marrow fat using chemical shift-encoding based water-fat MRI,"* J Magn Reson Imaging, vol. 42, no. 4, pp. 1018–1023, Oct. 2015.

The author contributed also to the following book chapters (ordered by year of appearance):

B1 T. Baum, D. C. Karampinos, **S. Ruschke**, H. Liebl, P. B. Noël, and J. S. Bauer, Osteoporosis in Computational Methods and Clinical Applications for Spine Imaging, Lecture Notes in Computational Vision and Biomechanics 18:67-93, 2015

The author contributed also to the following patent applications (ordered by year of appearance):

P1 **S. Ruschke**, D. C. Karampinos, H. Kooijman, H. Eggers, *Correction of concomitant gradient-induced phase errors in time-interleaved multi-echo gradient-echo imaging*, WO 2016180983 A1, Patent Application PCT/EP2016/060920, 13 May 2015

The author contributed also to the following conference abstracts (ordered by year of appearance):

C1 **S. Ruschke**, A. Pokorney, T. Baum, H. Eggers, J. H. Miller, H. H. Hu, and D. C. Karampinos, Measurement of vertebral bone marrow proton density fat fraction in children using quantitative water–fat MRI (**Young Investigator Award – 2nd prize**), Proc. of 34th Annual ESMRMB Meeting, p. 63, Barcelona, Spain, October 19-21, 2017 (oral presentation)

C2 **S. Ruschke**, A. Hock, D. Weidlich, E. J. Rummeny, J. S. Kirschke, T. Baum, R. Krug, D. C. Karampinos, Measuring fat unsaturation and polyunsaturation in vertebral bone marrow using dynamic inversion-recovery single-voxel spectroscopy, Proc. of 25th Scientific Meeting of ISMRM, p. 5115, Honolulu, Hawaii (USA), April 22-27, 2017 (electronic poster)

C3 D. J. Weidlich, A. Hock, **S. Ruschke**, D. Franz, K. Steiger, T. Skurk, H. Hauner, E. J. Rummeny, D. C. Karampinos, Probing bone marrow adipocyte cell size in vivo at a clinical 3 T scanner using high b-value DW-MRS at long diffusion times, Proc. of 25th Scientific Meeting of ISMRM, p. 1227, Honolulu, Hawaii (USA), April 22-27, 2017 (oral)

C4 M. N. Diefenbach, J. Meineke, P. Foehr, **S. Ruschke**, T. Baum, J. S. Kirschke, A. Hock, H. Kooijman, E. J. Rummeny, D. C. Karampinos, Simultaneous R2* and quantitative susceptibility mapping of trabecularized yellow bone marrow: initial results in the calcaneus, Proc. of 25th Scientific Meeting of ISMRM, p. 0850, Honolulu, Hawaii (USA), April 22-27, 2017 (oral)

C5 M. N. Diefenbach, **S. Ruschke**, D. C. Karampinos, A generalized formulation for parameter estimation in MR signals of multiple chemical species, Proc. of 25th Scientific Meeting of ISMRM, p. 5181, Honolulu, Hawaii (USA), April 22-27, 2017 (electronic poster)

C6 D. J. Weidlich, A. Hock, **S. Ruschke**, D. Franz, H. Hauner, E. J. Rummeny, D. C. Karampinos, Improving the quality of DW spectra in the supraclavicular fossa with a navigator-gated and cardiac-triggered flow-compensated diffusion-weighted STEAM MRS acquisition, Proc. of 25th Scientific Meeting of ISMRM, p. 5590, Honolulu, Hawaii (USA), April 22-27, 2017 (electronic poster)

C7 **S. Ruschke**, D. Weidlich, H. H. Hu, M. Diefenbach, H. Eggers, H. Kooijman, E. J. Rummeny, A. Haase, Jan S. Kirschke, T. Baum, D. C. Karampinos, Simultaneous T2, T2' and PDFF mapping in the spine using an adiabatic T2-prepared time-interleaved multi-echo gradient echo acquisition (**Magna Cum Laude Merit Award**), Proc. of 24th Scientific Meeting of ISMRM, p. 0568, Singapore, Singapore, May 7-13, 2016 (oral)

C8 **S. Ruschke**, H. Eggers, H. H. Hu, H. Kooijman, E. J. Rummeny, A. Haase, T. Baum, D. C. Karampinos, Bipolar time-interleaved multi-echo gradient echo imaging for high-resolution water-fat imaging, Proc. of 24th Scientific Meeting of ISMRM, p. 3264, Singapore, Singapore, May 7-13, 2016 (electronic poster)

C9 **S. Ruschke**, A. Pokorney, H. Eggers, J. S. Kirschke, T. Baum, D. C. Karampinos, H. H. Hu, Quantification of vertebral bone marrow fat fraction using time-interleaved multi-echo gradient-echo water-fat MRI: preliminary experience in children, Proc. of 24th Scientific Meeting of ISMRM, p. 4478, Singapore, Singapore, May 7-13, 2016 (electronic poster)

C10 M. N. Diefenbach, **S. Ruschke**, H. Kooijman, A. T. Van, E. J. Rummeny, A. Haase, D. C. Karampinos, Improving Chemical Shift-Encoded Water-Fat Separation Based On A Detailed Consideration Of Magnetic Field Contributions, Proc. of 24th Scientific Meeting of ISMRM, p. 0576, Singapore, Singapore, May 7-13, 2016 (oral)

C11 M. Dieckmeyer, **S. Ruschke**, H. Kooijman, E. J. Rummeny, J. S. Bauer, T. Baum, D. C. Karampinos, Comparison of vertebral bone marrow water ADC between young and old subjects: DW-MRS versus DWI, Proc. of 24th Scientific Meeting of ISMRM, p. 4463, Singapore, Singapore, May 7-13, 2016 (electronic poster)

C12 S. D. Sharma, D. Hernando, T. Yokoo, M. R. Bashir, J. Shaffer, Q. Yuan, **S. Ruschke**, D. C. Karampinos, J. H. Brittain, S. B. Reeder, Development And Multi-Center Validation Of A Novel Water-Fat-Iron Phantom For Joint Fat And Iron Quantification, Proc. of 24th Scientific Meeting of ISMRM, p. 3274, Singapore, Singapore, May 7-13, 2016 (electronic poster)

C13 T. Baum, S. Inhuber, M. Dieckmeyer, C. Cordes, **S. Ruschke**, E. Klupp, H. Eggers, H. Kooijman, E. J. Rummeny, A. Schwirtz, J. S. Kirschke, D. C. Karampinos, Association of quadriceps muscle fat with isometricstrength measurements in healthy males using chemical shift encoding-based water-fat MRI, Proc. of 24th Scientific Meeting of ISMRM, p. 0759, Singapore, Singapore, May 7-13, 2016 (oral)

C14 C. Cordes, T. Baum, J. Clavel, **S. Ruschke**, M. Dieckmeyer, D. Franz, H. Kooijman, E. J. Rummeny, H. Hauner, D. C. Karampinos, Subcutaneous fat unsaturation is negatively associated with liver fat fraction, Proc. of 24th Scientific Meeting of ISMRM, p. 3913, Singapore, Singapore, May 7-13, 2016 (electronic poster)

C15 **S. Ruschke**, D. Weidlich, M. N. Diefenbach, H. Eggers, H. Kooijman, Harry H. Hu, E. J. Rummeny, A. Haase, J. S. Bauer, T. Baum, D. C. Karampinos, Simultaneous T2, T2' and PDFF mapping using an adiabatic T2-prepared time-interleaved multi-echo gradient echo acquisition, ISMRM Workshop on Data Sampling and Image Reconstruction, P36, Sedona, Arizona, USA, January 17-20, 2016 (poster)

C16 T. Baum, **S. Ruschke**, C. Cordes, M. Dieckmeyer, H. Kooijman, R. Burgkart, E. J. Rummeny, J. S. Bauer, D. C. Karampinos. Association of MRS-based bone marrow fat fraction and unsaturation level with vertebral bone strength, 2016 European Congress of Radiology, B-0485, Vienna, Austria, March 2-6, 2014 (oral)

C17 **S. Ruschke**, H. Eggers, H. Kooijman, T. Baum, M. Settles, A. Haase, E. J. Rummeny, D. C. Karampinos, Addressing phase errors in quantitative water-fat imaging at 3 T using a time-interleaved multi-echo gradient-echo acquisition, (**Magna Cum Laude Merit Award**), Proc. of 23rd Scientific Meeting of ISMRM, p. 3657, Toronto, Canada, May 30-June 5, 2015 (electronic poster)

C18 **S. Ruschke**, H. Eggers, H. Kooijman, P. M. Jungmann, A. Haase, E. J. Rummeny, T. Baum, D. C. Karampinos, Chemical shift encoding-based water-fat imaging of skeletal muscle in the presence of fat resonance shift and phase errors, Proc. of 23rd Scientific Meeting of ISMRM, p. 3654, Toronto, Canada, May 30-June 5, 2015 (electronic poster)

C19 **S. Ruschke**, M. Dieckmeyer, H. Kooijman, A. Haase, E. J. Rummeny, J. S. Bauer, T. Baum, D. C. Karampinos, Separating water and olefinic fat peaks using diffusion-weighted MRS and diffusion constraint fitting to measure vertebral bone marrow fat unsaturation, Proc. of 23rd Scientific Meeting of ISMRM, p. 0618, Toronto, Canada, May 30-June 5, 2015 (oral)

C20 D. C. Karampinos, **S. Ruschke**, M. Dieckmeyer, H. Eggers, H. Kooijman, Ernst J Rummeny, J. S. Bauer, T. Baum, Comparison of T2* correction methods for vertebral bone marrow fat quantification using chemical shift encoding-based water-fat imaging, Proc. of 23rd Scientific Meeting of ISMRM, p. 0338, Toronto, Canada, May 30-June 5, 2015 (electronic poster)

C21 M. Dieckmeyer, **S. Ruschke**, C. Cordes, S. P. Yap, H. Kooijman, H. Hauner, E. J. Rummeny, J. S. Bauer, T. Baum, D. C. Karampinos, MRS-based vertebral bone marrow fat quantification using prior fat spectrum characterization and T2 correction, Proc. of 23rd Scientific Meeting of ISMRM, p. 0939, Toronto, Canada, May 30-June 5, 2015 (oral)

C22 M. Dieckmeyer, **S. Ruschke**, H. Eggers, H. Kooijman, E. J. Rummeny, J. S. Bauer, T. Baum, D. C. Karampinos, Removing the confounding effect of the fat component in ADC quantification of the vertebral bone marrow water component, Proc. of 23rd Scientific Meeting of ISMRM, p. 314, Toronto, Canada, May 30-June 5, 2015 (oral)

C23 C. Cordes, M. Dieckmeyer, B. Ott, J. Shen, **S. Ruschke**, M. Settles, C. Eichhorn, J. S. Bauer, H. Kooijman, E. J. Rummeny, T. Skurk, T. Baum, H. Hauner, D. C. Karampinos, Bone marrow fat behaves differently from abdominal fat, liver fat and serum lipids after a four-week calorie restriction in obese women, Proc. of 23rd Scientific Meeting of ISMRM, p. 4117, Toronto, Canada, May 30-June 5, 2015 (electronic poster)

C24 T. Baum, S. P. Yap, M. Dieckmeyer, **S. Ruschke**, H. Eggers, H. Kooijman, E. J. Rummeny, J. S. Bauer, D. C. Karampinos, Whole spine vertebral bone marrow proton density fat fraction mapping: anatomical variation and gender-specific reference database, Proc. of 23rd Scientific Meeting of ISMRM, p. 1216, Toronto, Canada, May 30-June 5, 2015 (traditional poster)

C25 **S. Ruschke**, T. Baum, H. Kooijman, M. Settles, A. Haase, E. J. Rummeny, and D. C. Karampinos, Diffusion-weighted STEAM MRS to measure fat unsaturation in regions with low fat content (**Magna Cum Laude Merit Award**), Proc. of 22nd Scientific Meeting of ISMRM, p. 3601, Milan, Italy, May 10-16, 2014 (electronic poster)

C26 **S. Ruschke**, T. Baum, H. Kooijman, M. Settles, A. Haase, E. J. Rummeny, and D. C. Karampinos, Eddy current correction in diffusion-weighted STEAM MRS in the presence of water and fat peaks, Proc. of 22nd Scientific Meeting of ISMRM, p. 2268, Milan, Italy, May 10-16, 2014 (traditional poster)

C27 D. C. Karampinos, **S. Ruschke**, H. Eggers, M. Settles, H. Kooijman, P.Boernert, E. J. Rummeny, T. Baum, On the need for T2* correction in quantitative water-fat imaging of skeletal muscle, Proc. of 22nd Scientific Meeting of ISMRM, p. 4276, Milan, Italy, May 10-16, 2014 (electronic poster)

C28 T. Baum, **S. Ruschke**, O. Gordijenko, E. Grande Garcia, H. Kooijman, R. Burgkart, Ernst J Rummeny, J. S. Bauer, and D. C. Karampinos, Linkage of vertebral bone marrow fat content with biomechanical strength and trabecular bone structure parameter, Proc. of 22nd Scientific Meeting of ISMRM, p. 0507, Milan, Italy, May 10-16, 2014 (oral)

# Contents

# 1 Introduction

Tomographic imaging modalities allow to take a glance on the internal structure of the human body and are therefore an integral part of modern medicine. Among many existing techniques, magnetic resonance imaging (MRI) may be the most fascinating one allowing the non-invasive measurement of manifold contrasts. Particularly, the absence of ionizing radiation makes MR a valuable tool in both clinical and research settings.

In contrast with most other modalities, the signal detected in MRI emerges from the tissue itself and is not emitted externally. For example, computed tomography (CT) measures the attenuation of generated by X-ray beams during tissue penetration. However, not all nuclei can be examined using magnetic resonance (MR). In fact most signal in clinical scanning arises from $^{1}$H nuclei bound in water and fat molecules. The signal characteristics of the imaged $^{1}$H nuclei differ depending of their molecular environment which leads to e.g. a specific contrast between water and fat. The water signal has been traditionally in the focus of clinical interest. That is why a lot of effort was put into the suppression of the fat signal or the separation of the water from the fat signal in routine clinical imaging.

The signal of $^{1}$H nuclei bound in water can be differentiated from $^{1}$H nuclei bound in fat based on their intrinsic resonance frequencies, also known as chemical shift. The corresponding MR imaging technique is referred to as chemical shift encoding-based imaging, water–fat imaging or Dixon imaging. The technique was named after Thomas Dixon who for the first time described in 1984 the idea of encoding the chemical shift information in an imaging experiment [1]. Furthermore, quantitative water–fat imaging allows not only the separation of water and fat signals but also enables the measurement of the proton density fat fraction (PDFF) which has evolved to a promising imaging biomarker. Therefore, quantitative water–fat imaging has been used in the assessment of tissue fat content in numerous clinical applications such as the characterization of metabolic disorders [2–4], hepatic steatosis [5] and cancer [6, 7]. However, achieving robust and accurate quantitative measurements using quantitative water–fat imaging is challenging as several confounding factors have to be addressed.

While MRI is focusing on the encoding of spatial information, magnetic resonance spectroscopy (MRS) is aiming for encoding information in the chemical shift dimension. Therefore, MRS allows not only to extract the PDFF but also to extract addtional characteristic triglyceride parameters which e.g. refer to the degree of (un)saturation of the fatty acids within triglycerides [8]. However, quantitative MRS aiming for the measurement of the degree of (un)saturation of triglycerides relies on the extraction of chemical shift components of triglycerides close to the chemical shift of water and is therefore non trivial in the presence of a strong water signal, e.g. in muscle tissue.

## 1.1 Clinical Relevance

Natural lipids in the form of triglycerides are essential to the human organism as they fulfill central functions. Triglycerides serve for example as energy subtrates and precursor signaling molecules or other essential lipids [9, 10]. The accumulation of triglycerides plays an important

role in many diseases.

While the role of adipose tissue may be obvious in diseases like the metabolic syndrome [11–13] its role becomes less clear for example in osteoporosis where the gardual conversion of hematopoetic bone marrow into adipocyte rich bone marrow is not entirely understood [14–19].

Metabolic syndrome is a cluster of medical conditions [20] and associated with an increased risk for developing cardiovascular disease [21] and type 2 diabetes [22]. Although metabolic syndrome can be diagnosed based on the body mass index and blood glucose levels, the optimal prevention strategies against cardiovascular disease and diabetes remain challenging [23–26]. Proposed imaging biomarkers investigating the triglyceride content of for example visceral adipose tissue [27, 28] or intrahepatic fat [29, 30] were shown to correlate with insulin resistance, respectively.

Osteoporosis is defined as a metabolic bone disease characterized by reduced load capacity due to structural deterioration leading to an increased fracture risk [31]. Osteoporosis induced fractures may reduce not only the quality of life [32] but also correlate with an increased mortality [33]. Furthermore, the additional socioeconomic burden of osteoporosis is estimated to be enormous based on the expected demographical changes [34]. Osteoporosis can be treated with medications, but it's early diagnosis remains insufficient and suffers from limited precision of prediction [35–37] based on bone mineral density [38]. The cavities of trabecular bone contain bone marrow which consists of a hematopoetic component and adipocytes. Recent work has shown a negative correlation of bone marrow fat fraction [39–43] and bone marrow fat unsaturation [39, 44] with bone mineral density, respectively. Furthermore bone marrow fat fraction was also reported to correlate with the prevalence of a vertebral fracture after adjustment for bone mineral density [19].

Metabolic syndrome and osteoporosis are two exemplary complex and challenging diseases where quantitative MR-based biomarkers measuring triglyceride content or fatty acid composition of triglycerides may help to better understand underlying metabolic mechanisms of triglycerides and may contribute to improve diagnostic performance.

## 1.2 Thesis Purpose

The overall purpose of the present dissertation is the development of an MRS-based method to quantify triglyceride (un)saturation in musculoskeletal tissues with low fat content and of an MRI-based method for quantitative PDFF measurements plus its application in the assessment of vertebral bone marrow PDFF in children. Therefore, the thesis can be divided into two major parts. First, the utilization of an optimized diffusion-weighted stimulated echo acquisition mode (DW-STEAM) MR spectroscopy sequence is proposed to assess the triglyceride (un)saturation in tissues with low PDFF. Second, the development of a phase error correction scheme for accurate and robust quantitative chemical shift encoding-based monopolar water–fat imaging is introduced. Its application to measure the vertebral bone marrow PDFF in pediatrics to examine cross-sectional changes with age and intra-individual variations from the lumbar to the cervical region in the first two decades of life is then described.

## 1.3 Thesis Structure

The present cumulative thesis aims to describe the methodological foundation and to provide an overall discussion of the three embedded journal publications in the context of existing literature.

The methodological foundation in the context of the embedded journal publications is given in Chapter 2. A short overview of the physical background and employed techniques in magnetic resonance spectroscopy and imaging are given in Chapter 2 followed by a brief description of the employed techniques in Chapters 3 to 5. Summaries of the three embedded journal publications can be found in Chapter 7. Finally, an overall discussion on the implications of the present work and its literature context is given in Chapter 8.

# 2 Magnetic Resonance in Medicine

This chapter briefly summarizes the physical background and technical basics of the present work.

## 2.1 Physical Principles

Nuclear magnetic resonance (NMR) allows the non-invasive excitation of nuclei in a magnetic field and the measurement of the re-emitted electromagnetic radiation, which is specific to the quantum mechanical properties of the nuclei. All isotopes consisting of an odd number of protons and / or neutrons have an intrinsic magnetic and angular moment which is required for NMR. The transitions between the nuclear spin levels can be observed in an NMR experiment. In contrast to disciplines within the field of natural science the word "nuclear" is dropped in the medical context and MR is used to refer to this concept. In the following the medical nomenclature will be used. Although a lot of isotopes theoretically qualify to be measured using MR, only the $^1$H nuclei is usually considered in the medical context due to its high abundance in biological tissues.

### 2.1.1 Magnetic Resonance

The phenomenon of NMR is usually explained using either quantum mechanics, classical mechanics or a combination of both. However, since a large number of nulcei – also referred to as spin ensemble – is typically involved in an MR experiment the classical mechanical description is in general sufficient [45] and briefly recapitulated in the following:

The intrinsic angular moment $\boldsymbol{A}$ of a spin ensemble induces a magnetic moment $\boldsymbol{M}$ according to

$$\boldsymbol{M} = \gamma \boldsymbol{A} \tag{2.1}$$

where $\gamma$ is the isotope's specific gyromagnetic ratio. In the case of the $^1$H nuclei the gyromagnetic ratio has the value of $\gamma/2\pi = \gamma = 42.58\,\mathrm{MHz\,T^{-1}}$.

In the presence of a magnetic field $\boldsymbol{B}$, the magnetic moment $\boldsymbol{M}$ will then experience a torque $\boldsymbol{\tau}$:

$$\boldsymbol{\tau} = \boldsymbol{M} \times \boldsymbol{B} = \frac{d\boldsymbol{A}}{dt} \tag{2.2}$$

As a result from (2.1) and (2.2) the change of the magnetic moment over time yields

$$\frac{d\boldsymbol{M}}{dt} = -\gamma \boldsymbol{M} \times \boldsymbol{B} \tag{2.3}$$

As it can be seen from (2.3), the magnetic moment has a constant amplitude and only experiences changes perpendicular to its vector.

The relationship between the precession frequency $\omega$ as a result of the magnetic moment $\boldsymbol{M}$ experiencing a static magnetic field $B_0$ is also known as Larmor equation and given by

$$\omega_0 = -\gamma B_0 \tag{2.4}$$

The characteristic frequency $\omega_0$ is called Larmor frequency.

### 2.1.2 Excitation

Using the Cartesian representation, the magnetic field vector $\boldsymbol{B}$ consists of the static magnetic field $B_0$ along the longitudinal axis and the $B_1$ field oscillating at the Larmor frequency $\omega_0$ in the transverse plane yields

$$\boldsymbol{B} = \begin{pmatrix} -B_1 \sin(-\gamma B_0 t) \\ B_1 \cos(-\gamma B_0 t) \\ B_0 \end{pmatrix} \tag{2.5}$$

In (2.5), the static main magnetic field $B_0$ was defined parallel to the z-axis of the Cartesian coordinate system in accordance with the usual MR conventions. Due to this convention the z-axis is also referred to as longitudinal axis, while the xy-plane is called transverse plane. This nomenclature is also used to differentiate two different relaxation phenomena in Section 2.1.3.

The solution to (2.3) with inserted magnetic field vector (2.5) can be derived from the solution to general decoupled first-order differential equations. After setting the initial conditions to the equilibrium state ($\boldsymbol{M}(t=0) \parallel B_0$, see also Section 2.1.3) the time dependent magnetization vector $\boldsymbol{M}(t)$ can then be retrieved as

$$\boldsymbol{M}(t) = M_0 \begin{pmatrix} \cos(-\gamma B_0 t)\sin(-\gamma B_1 t) \\ \sin(-\gamma B_0 t)\sin(-\gamma B_1 t) \\ \cos(-\gamma B_1 t) \end{pmatrix} \tag{2.6}$$

$M_0$, the amplitude of the magnetization vector can be estimated by the first order approximation of the Boltzmann distribution:

$$M_0 = \rho \frac{\gamma^2 \hbar^2}{4 k_B T} B_0 \tag{2.7}$$

where $\rho$ is the spin density, $\hbar$ is the reduced Planck constant, $k_B$ is the Boltzmann constant and $T$ is the temperature.

### 2.1.3 Relaxation

Two different types of relaxation are used to phenomenologically describe how a spin ensemble approaches its equilibrium magnetization:

- The Spin–lattice interaction describes a mechanism by which the longitudinal component of the magnetization exponentially decays with a characteristic relaxation time $T_1$ towards its thermodynamic equilibrium with its surrounding atoms and molecules.

- The Spin–spin interaction describes a mechanism by which the transverse component of the magnetization exponentially decays with a characteristic relaxation time $T_2$ towards its equilibrium.

Inserting the effect of relaxation into (2.3) yields the famous Bloch equation named after Felix Bloch:

$$\frac{d\boldsymbol{M}}{dt} = \gamma \boldsymbol{M} \times \boldsymbol{B} + \begin{pmatrix} -\frac{M_x}{T_2} \\ -\frac{M_y}{T_2} \\ -\frac{M_z - M_0}{T_1} \end{pmatrix} \tag{2.8}$$

where $M_x$, $M_y$ and $M_z$ are the three spatial components of the magnetization vector. To be able to observe the effect of relaxation the magnetization has to transit from a non-equilibrium state to its equilibrium state. Assuming the absence of any $B_1$ field and the magnetization vector being parallel to the x-axis at $t = 0$ the solution to (2.8) can be derived similar to (2.3) and results in

$$\boldsymbol{M}(t) = M_0 \begin{pmatrix} \cos\left(-\gamma B_0 t\right) e^{-\frac{t}{T_2}} \\ \sin\left(-\gamma B_0 t\right) e^{-\frac{t}{T_2}} \\ 1 - e^{-\frac{t}{T_1}} \end{pmatrix} \tag{2.9}$$

The effective transverse relaxation time $T_2^*$ is another quantity that can be measured with MR. $T_2^*$ describes the combination of the transverse relaxation time $T_2$ and the presence of local magnetic field inhomogeneities $\Delta B_i$ which lead to a second time component denoted as $T_2'$:

$$\frac{1}{T_2^*} = \frac{1}{T_2} + \gamma \Delta B_i = \frac{1}{T_2} + \frac{1}{T_2'} \tag{2.10}$$

By its definition given in (2.10), $T_2^*$ is always shorter than or equal to $T_2$. The main characteristic that distinguishes $T_2'$ from $T_2$ is that the $T_2'$ signal is reversible (recoverable) while $T_2$ is irreversible (nonrecoverable).

When relaxation rates are used instead of the relaxation times ( $R = T^{-1}$ ) Equation (2.10) can be rewritten as

$$R_2^* = R_2 + R_2' \tag{2.11}$$

where the effective transverse relaxation rate $R_2^*$ is the sum of the intrinsic relaxation rate $R_2$ and the decay rate due to magnetic field inhomogeneities $R_2'$.

### 2.1.4 Chemical Shift

The term chemical shift refers to the effect that the same nucleus in different chemical environments resonates at different precession frequencies. The actual experienced static magnetic field $B_{eff}$ of the nucleus is slightly lower owing to the shielding effect of surrounding electron clouds and can be given by

$$B_{eff} = B_0 \left(1 - \sigma\right) \tag{2.12}$$

where $\sigma$ is the shielding constant describing the effect shielding effect.

The actual precession frequency $\omega$ is then

$$\omega = -\gamma B_{eff} = -\gamma B_0 \left(1 - \sigma\right) \tag{2.13}$$

Hence the precession frequency of a nucleus is reflecting its local environment and the chemical structure the nucleus is embedded in. The chemical shift $\delta_{ppm}$ is given in the unit of parts per million (ppm) and is defined as

$$\delta_{ppm} = \frac{f - f_{ref}}{f_{ref}} 10^6 \tag{2.14}$$

where $f$ and $f_{ref}$ are the resonance frequency and the reference frequency, respectively. By definition, the chemical shift of $^1$H is measured relative to the reference frequency of tetramethylsilane (TMS). For example, the chemical shift of protons bound in water molecules at 37 °C is approximately 4.67 ppm.

### 2.1.5 Concomitant Gradient Field

Spatially varying magnetic gradient fields are used in MRI to achieve for example spatial encoding (Section 2.2.6) or to create gradient echoes (Section 2.2.3). Whenever a linear magnetic field gradient is applied it is accompanied by a nonlinear spatially dependent magnetic field called concomitant gradient field. The concomitant gradient field can be derived from Maxwell's equations for divergence and curl of magnetic fields in free space stating

$$\boldsymbol{\nabla} \cdot \boldsymbol{B} = 0 \tag{2.15}$$

and

$$\boldsymbol{\nabla} \times \boldsymbol{B} = 0 \tag{2.16}$$

, respectively.

As previsouly shown by Bernstein et al. [46], the concomitant gradient field to the lowest order $B_{cg}$ can be described by

$$\begin{aligned} B_{cg}\left(x,y,z,t\right) = \frac{1}{2B_0} \Bigg\{ & G_x\left(t\right)^2 z^2 + G_y\left(t\right)^2 z^2 + G_z\left(t\right)^2 \frac{x^2+y^2}{4} \\ & - G_x\left(t\right) G_z\left(t\right) xz - G_y\left(t\right) G_z\left(t\right) yz \Bigg\} \end{aligned} \tag{2.17}$$

where $G_x$, $G_y$ and $G_z$ denote the applied magnetic gradient filed in $x$, $y$ and $z$ direction as a function of time, respectively.

The concomitant field phase $\Phi_{cg}$ caused by the concomitant gradient field to the lowest order $B_{cg}$ yields then

$$\Phi_{cg}\left(x,y,z\right) = \gamma \int B_{cg}(x,y,z,t)dt \tag{2.18}$$

The additional phase due to the concomitant field phase vanishes towards the iso-center ($x$,$y$,$z \to 0$) and gets stronger towards off-iso-center. The concomitant field phase $\Phi_{cg}$ also scales inversely with the static magnetic field $B_0$.

## 2.2 Generation of a Magnetic Resonance Signal

In order to generate a detectable MR signal, a sample has to be probed that contains isotopes with the mentioned quantum mechanical properties, e.g. a sample with $^1$H nuclei. This sample is then placed in a strong static magnetic field $B_0$. $B_0$ is usually in the order of several Tesla, e.g.

at 3 T the $^1$H nuclei precess at a Larmor frequency of $\gamma B_0 = 42.58\,\mathrm{MHz\,T^{-1}} \times 3\,\mathrm{T} = 127.7\,\mathrm{MHz}$. Whenever spins are in a non-equilibrium state they will relax to equilibrium after some time in the static $B_0$ field. The equilibrium state is the initial state an MR experiment starts from. The spins can then be excited by applying the transverse $B_1$ field at the Larmor frequency of the spins. The $B_1$ field is also referred to as radio frequency pulse (RF pulse) and the angle of the rotation of the magnetization vector is called flip angle $\theta$, while its causing RF pulse is then also named as $\theta$°-pulse. In the simple case of a 90°-pulse the magnetization vector will precess to the transverse plane and thus induce an electric current in nearby conducting materials according to Faraday's law of induction. The induced current can then be picked up by nearby receiver coils. The receiver coils are orthogonally paired coils and enable the reception of a complex signal corresponding to the transverse magnetic moment as a function of time (quadrature detection). The created signal will then decay with it's characteristic $T_2^*$-decay and is termed free induction decay (FID). The timing diagram describing how an FID signal is formed is shown in Figure 2.1.

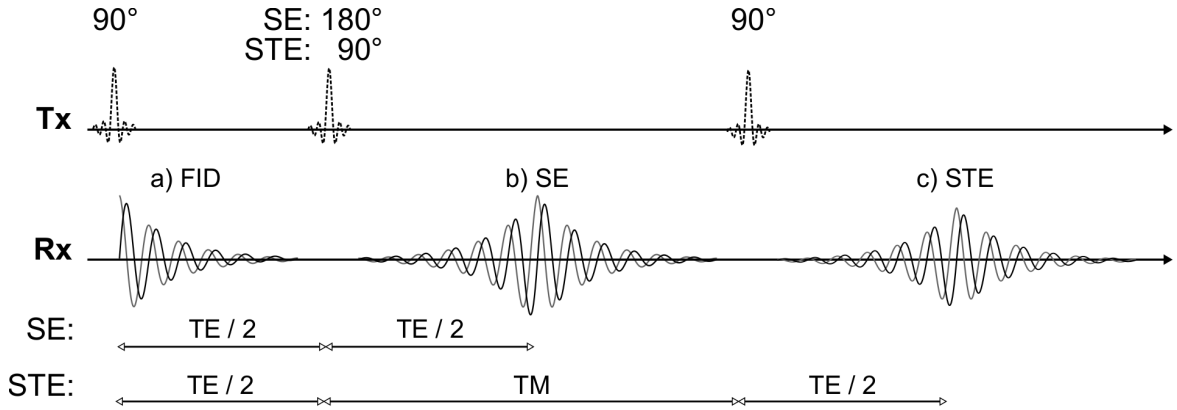


**Figure 2.1:** Generation of an MR signal: a) A free induction decay (FID) signal with $T_2^*$-decay is generated after applying a 90°-pulse. b) A (primary) spin echo (SE) is generated by applying a 180°-pulse after a 90°-pulse. c) A stimulated echo (STE) is generated e.g. by applying three consecutive 90°-pulses. Two primary SEs and one secondary SE that are generated after the third RF pulse, as well as the FIDs generated after the second and third RF pulse, respectively, are not shown. The gray and black signal curves represent the real and imaginary component of the complex signal, respectively. Tx, transmission; Rx, reception; TE, echo time; TM, mixing time; RF pulse, radio frequency pulse.

### 2.2.1 Spin Echoes

A spin echo can be created if the transverse magnetization, which was flipped by e.g. using a 90°-pulse, gets refocused on the transverse plane by applying a second RF pulse with a flip angle of 180°. The 180°-pulse inverts the relative phase of the spins in the transverse plan. This causes a refocusing of of the magnetization vector and leads to a spin echo as it is depicted in Figure 2.1. The time interval between the 90°-pulse until the occurrence of the echo is called echo time (TE). It is defined by the interval between the 90°-pulse and the refocusing 180°-pulse which equals half of the TE.

### 2.2.2 Stimulated Echoes

A stimulated echo can be created by applying multiple non-180° refocusing pulses. In the most basic case three consecutive 90°-pulses are used to tip the magnetization into the transverse plane after the first, to the negative longitudinal axis using the second pulse and back to the transverse plane using the third pulse, respectively. The first pulse creates an FID with its characteristic $T_2^*$-decay, followed by the second pulse inverting the magentization and the magnetization being now subject to $T_1$ relaxation. Finally, the third echo produces the stimulated echo by rephasing the magnetization. The duration between the second and third pulse is called mixing time (TM) and controls the $T_1$-weighting of the signal. The durations between the first and second pulse and between the third pulse and the occurrence of the stimulated echo are responsible for $T_2$-weighting and correspond the TE. The corresponding sequence is denoted as stimulated echo acquisition mode (STEAM) [47].

### 2.2.3 Gradient Echoes

Gradient echoes are formed using magnetic field gradients as opposed to RF pulses which are used to generate FIDs, spin echoes and stimulated echoes. However, an RF pulse is used for the initial excitation. The excitation is followed by a dephasing gradient and finally by the readout gradient. The characteristic echo time is defined as the duration between the RF excitation until the formation of the gradient echo. The generated echo signal is subject to $T_2^*$-decay. Additional consecutive gradient echoes can be formed by adding readout gradients with alternating polarity to the end of the readout.

### 2.2.4 Magnetic Resonance Pulse Sequences

MR pulse sequences consist of a sequential arrangement of RF pulses and gradient waveforms. Pulse sequences can be designed to achieve different contrasts, motion insensitivity, scan time, high signal-to-noise ratio (SNR), quantitative imaging and many more goals. In general, experimental design in MRI relies on a trade-off between resolution, SNR and total scan time. Therefore the purpose of the measurement has to be well defined before an experiment can be performed. Furthermore, all pulse sequences need a tailored reconstruction method (Section 2.2.7) that is able to transform the measured raw data into valuable information. Traditionally, a pulse sequence consists of a repetitive pattern with a constant duration including the excitation of spins followed by a part for signal reception. This constant duration of the repetition interval is called repetition time (TR). The TR can either be chosen large enough that the magnetization has time to recover back to equilibrium or the sequence has to be designed to operate in a steady state or pseudo steady state mode [48]. In gradient echo-based imaging, TR is often much shorter than $T_1$ and often also smaller than $T_2$.

In chemical shift encoding-based gradient-echo-based water–fat imaging, a technique called spoiled gradient echo (SPGR) is mostly employed where the residual transverse magnetization gets dephased at the end of each TR. In SPGR, steady state needs only to be achieved for the longitudinal magnetization. Other techniques without spoiling rely on matched or nulled gradient moments in each TR and are called steady state free precession (SSFP) and balanced SSFP (bSSFP), respectively. Non-spoiled sequences have the advantage of higher SNR. The drawbacks of non-spoiled sequences are their sensitivity to off-resonance effects and a signal evolution depending on both $T_1$ and $T_2$. Recently, a new approach named magentic resonance fingerprinting (MRF) [49] has been proposed using pseudorandomized parameters

including flip angle and TR to differentiate tissue properties including $T_1$ and $T_2$ based on their characteristic signal evolution.

### 2.2.5 The concept of k-space

The complex signal acquired during an MRI experiment is obtained in the frequency domain also known as k-space domain, or k-space. The relationship between the observed k-space signal $S(\boldsymbol{k})$ and the image function representation in the spatial domain $\rho(\boldsymbol{r})$ can be expressed in form of a Fourier transform via

$$S(\boldsymbol{k}) = \int_{-\infty}^{+\infty} \rho(\boldsymbol{r})\, e^{-i2\pi(\boldsymbol{k}\cdot\boldsymbol{r})} \mathrm{d}^3\boldsymbol{r} \tag{2.19}$$

with $\boldsymbol{k} = [k_x, k_y, k_z]^T$ and $\boldsymbol{r} = [x, y, z]^T$ being the k-space vector and spatial vector, respectively.

### 2.2.6 Spatial Encoding

Spatial encoding has to be applied in order to extract images or maps from the acquired signal. A spatially varying magnetic field is used to distinct between nuclei that have the same intrinsic chemical shift but a different location. The spatially varying magnetic field is created by the gradient coils. Three pairs of orthogonal gradient coils - one pair for each physical axis of the scanner - allow to dynamically add additional magnetic fields which vary approximately linearly along their axis. The gradient coil-induced magnetic fields are much smaller compared to the static magnetic field and have usually a strength of the order of up to $40\,\mathrm{mT\,m^{-1}}$ at $3\,\mathrm{T}$ on a whole-body scanner. Linear combinations of the three gradient axis allow to vary the magnetic field along arbitrary directions. The resulting spatially varying magnetic field yields a spatially varying resonance frequency of the nuclei under investigation and thus allows spatial encoding of the received signal.

A simple example of retrieving a (partially or 1D) spatially resolved signal is the use of a technique called slice-selection which is used in 2D or multi-slice imaging. Slice-selection can by achieved be applying an RF pulse with a limited bandwidth in the presence of a magnetic gradient field. The RF pulse then only excites spins which have a resonance frequency within the excitation bandwidth of the pulse. The Larmor frequency at a spatial position $z$ in presence of a magnetic gradient field $G_z$ is then given by:

$$\omega(z) = \omega_0 + \gamma G_z z \tag{2.20}$$

Moreover, most 3D imaging techniques and single-voxel spectroscopy make use of the same principle to excite one or multiple slabs, and are therefore referring to this approach as slab selection.

Finally, further spatial encoding of additional dimensions can be achieved by adjoining perpendicular phase encoding dimensions, e.g. 2D imaging usually includes one phase encoding direction and 3D imaging usually includes two phase encoding directions. Phase encoding is realized by turning on a magnetic gradient field $G_x$ for a short time interval $T_{pe}$ after performing an RF excitation-pulse. Consequently the signal acquired afterwards has an accumulated initial phase angle $\phi(x)$:

$$\phi(x) = -\gamma G_x x T_{pe} \tag{2.21}$$

The signal is called phase-encoded since $\phi(x)$ has a linear relationship to the signal location $x$, as it can be seen from Equation (2.21).

### 2.2.7 Image Reconstruction

The process of converting the measured raw data to images and maps is called image reconstruction and may also include additional post-processing steps. The raw data is acquired in the k-space domain and therefore has to be transformed into the image space domain.

A simple example would be a regular rectangular sampled grid in k-space that is discrete Fourier transformed (DFT) into image space. The corresponding DFT can then be defined by

$$X_{\mathbf{k}} = \sum_{\mathbf{n}=0}^{\mathbf{N}-1} r_{\mathbf{n}} e^{-2\pi i \mathbf{k}\cdot(\mathbf{n}/\mathbf{N})} \tag{2.22}$$

which describes the transformation of the array $r_{\mathbf{n}}$ with $\mathbf{n} = (n_1, \ldots, n_d)$ being a $d$-dimensional vector of indices by a set of $d$ nested summations (over $n_j = 0 \ldots N_j - 1$ for each $j$) with element-wise operation of $\mathbf{n}/\mathbf{N} = (n_1/N_1, \ldots, n_d/N_d)$.

Moreover, since the gradient coils allow arbitrary sampling patterns, also referred to as k-space trajectories, not only Cartesian sampled grids can be employed for signal encoding but also non-Cartesian patterns like spirals can be used. Non-Cartesian k-space data can then not be reconstructed using the DFT anymore. Nevertheless, Cartesian k-space trajectories were used throughout the entire work of this thesis.

### 2.2.8 Acquisition Acceleration, Parallel Imaging and Compressed Sensing

Compared to other modalities like CT, MRI is an intrinsic slow imaging technique. Clinical routine examinations including several image sets and different types of contrasts usually take 20 min to 60 min. A lot of effort has been put into accelerating MR acquisition times. Early approaches tried to improve the sampling efficiency based on the pulse sequence design as for example in echo planar imaging (EPI) where the entire k-space trajectory is sampled within a single TR, or using a Carr-Purcell-Meiboom-Gill (CPMG) [50, 51] sequence using phase encoding for each generated spin echo known as turbo spin echo (originially called rapid acquisition with refocused echoes (RARE)[52]) or the combination of both aforementioned techniques which is then called gradient and spin echo (GRASE)[53]. Another idea uses a small flip angle - also known as Ernst angle - to maximizing a pseudo steady state signal for a given TR much shorter than the tissue's $T_1$ relaxation, which is widely known as fast low angle shot (FLASH) [54]. Furthermore, more efficient k-space trajectories compared to the traditional Cartesian trajectory such as spirals have been proposed to improve the readout efficiency [55]. All the above mentioned techniques require the sampling of the entire k-space, which means that all phase encoding steps have to be performed. Especially in the last decades, when improved scanner hardware became available the physiological limits of conventionally increasing the sampling speed have been reached with peripheral nerve stimulation (PNS) and sometimes also the specific absorption rate (SAR) becoming a safety concern.

With the increasing number of available receive coil channels on clinical systems, several approaches in the area of parallel imaging were developed recently. Parallel imaging refers to the simultaneous signal reception using multiple coils allowing a coil channel sensitivity driven reconstruction of an under-sampled k-space. Most commonly used methods include

SMASH[56], SENSE[57], GRAPPA[58] and ESPRiT[59]. These methods can be differentiated based on the reconstruction domain they are performed in. SMASH and GRAPPA are performed in the k-space domain, SENSE is performed in the image domain and ESPRiT is a combination of the latter two. The present work makes partly use of the SENSE method especially for in vivo imaging to keep scan times reasonable. Recently, also the application of compressed sensing [60] was proposed for the reconstruction of under-sampled k-space data by introducing sparsity constrains - e.g. maximizing the sparsity - during reconstruction [61]. Many of the aforementioned acceleration methods can be combined to achieve even higher acceleration rates.

## 2.3 Hardware in Clinical MR Systems

Clinical MR scanners are predominantly whole-body scanners that are designed to allow the imaging of all body regions from head to foot. These scanners usually consist of a few main components, of which the magnet, the radio frequency coils and gradient coils along with computer systems for hardware controlling and image reconstruction are the most important ones. A clinical MR scanner usually requires a special installation ensuring a constant room temperature and additional electromagnetic-shielding (Faraday cage) to avoid electromagnetic inference with the environment. Due to the strong magnetic field of the main magnet of nowadays usually 1.5 T, 3 T or even up to 7 T, only MR compatible items can enter the scanner room.

### 2.3.1 Magnet

The main magnet creates a strong and static magnetic field, usually referred to as $B_0$-field. Clinical field strengths usually range from under 1 T to 1.5 T and 3 T up to 7 T. For comparison: the magnetic field on the surface of the earth ranges approximately from 0.25 $\mu$T to 0.65 $\mu$T. Super-conducting electromagnets are used in order to achieve such strong magnetic fields by exploiting the material's (e.g. niobium-titanium (NbTi)) superconducting property at very low temperatures below 10 K. Therefore a cryogenic cooling fluid such as liquid helium is required. Homogeneity of the magnetic field is a major quality criterion as it plays an important role for the achievable image quality. The process of optimizing the magnet's homogeneity is referred to as shimming where small metal plates and electrical shim coils are incorporated into the magnet. While the metal plates serve as constant shimming and are fixed during installation and cannot be altered easily, the shim coils serve as a dynamic shim component and can be adjusted for each patient individually to improve the uniformity of the magnetic field.

### 2.3.2 Radio Frequency Coils

The radio frequency coils are used for excitation by generating the $B_1$ field and also for signal detection. Usually a body coil, which is built inside the gantry is employed for excitation and smaller body-part-specific surface coil arrays that are put as close as possible to the region of interest are used for reception.

### 2.3.3 Gradient Coils

Three pairs of gradient coils are used to create three orthogonal gradient fields. Their main purpose is spatial encoding and the generation of gradient echoes, but they can also be used

for other purposes, such as diffusion encoding. The performance of the gradient system is usually characterized by its maximum gradient strength and gradient slew rate.

### 2.3.4 Experimental Setup

All experiments of the present thesis were performed on clinical whole-body 3 T MRI scanners (Ingenia, Philips Healthcare, The Netherlands) at the University Hospital Klinikum rechts der Isar of the Technical University of Munich in Munich (Germany) and at the Phoenix Children's Hospital in Phoenix, Arizona (USA).

# 3 Quantification and Characterization of Triglycerides with Magnetic Resonance

Triglycerides (or triacylglycerides) are the predominate constituent of human body fat. A triglyceride consists of three fatty acids esterified with glycerol. Fatty acids can be further divided into different types according to their chemical structure. In MRI often three main fatty acid groups are differentiated based on the number of double bonds in the carbon chain: Saturated, mono-unsaturated and poly-unsaturated fatty acids. The characteristics of the $^1$H spectrum of triglycerides are well known and allow the mapping of resonance frequencies – also known as chemical shifts – on the proton position within the triglyceride. The chemical structure of an exemplary triglyceride is given in Figure 3.1. Figure 3.2 shows a spectrum of vegetable corn oil acquired at 3 T on a clinical system. The capital letters A–J map the corresponding protons in the chemical structure (Figure 3.1) to their arising chemical shift (Figure 3.2). The glycerol backbone has five protons giving rise to three distinct frequencies (2 x G, 2 x H and 1 x I). All fatty acids show at least four distinct frequencies (A: methyl, B: methylene, C: $\beta$-carboxyl and E: $\alpha$-carboxyl), mono-unsaturated fatty acids show two additional frequencies (D: $\alpha$-olefinic and J: olefinic) and poly-unsaturated fatty acids have one further frequency (F: diallylic). The above model is already a simplification, as it assumes the presence of singlets only and neglects spin couplings leading to distinct splitting patterns. One example of these splitting patters is the triplet of the methyl peak (A) as it can be depicted from Figure 3.2. However, achievable linewidths at 3 T and in vivo usually do not allow the detection of multiplets.

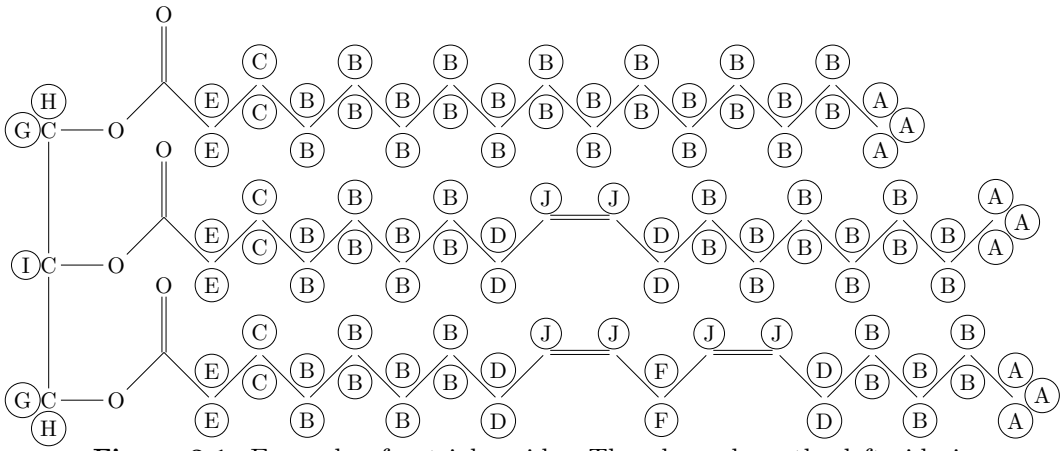

**Figure 3.1:** Example of a triglyceride: The glycerol on the left side is esterified with palmitic acid(16:0), oleic acid(18:1, 9$c$) and linoleic acid(18:2, 9$c$, 12$c$) on the right side (from top to bottom). The circled letters (A-J) label and group the protons according to their specific resonance frequency.

As described by Hamilton et al.[62], a mixture of saturated, mono-unsaturated and poly-

unsaturated triglycerides can be characterized by three parameters: the number of double bonds per triglyceride (ndb), the number of methylene-interrupted double bonds per triglyceride (nmidb) and the mean fatty acid carbon chain length (CL). The relationship between the parameters ndb, nmidb and CL and the ten peaks A–J is summarized in Table 3.1.

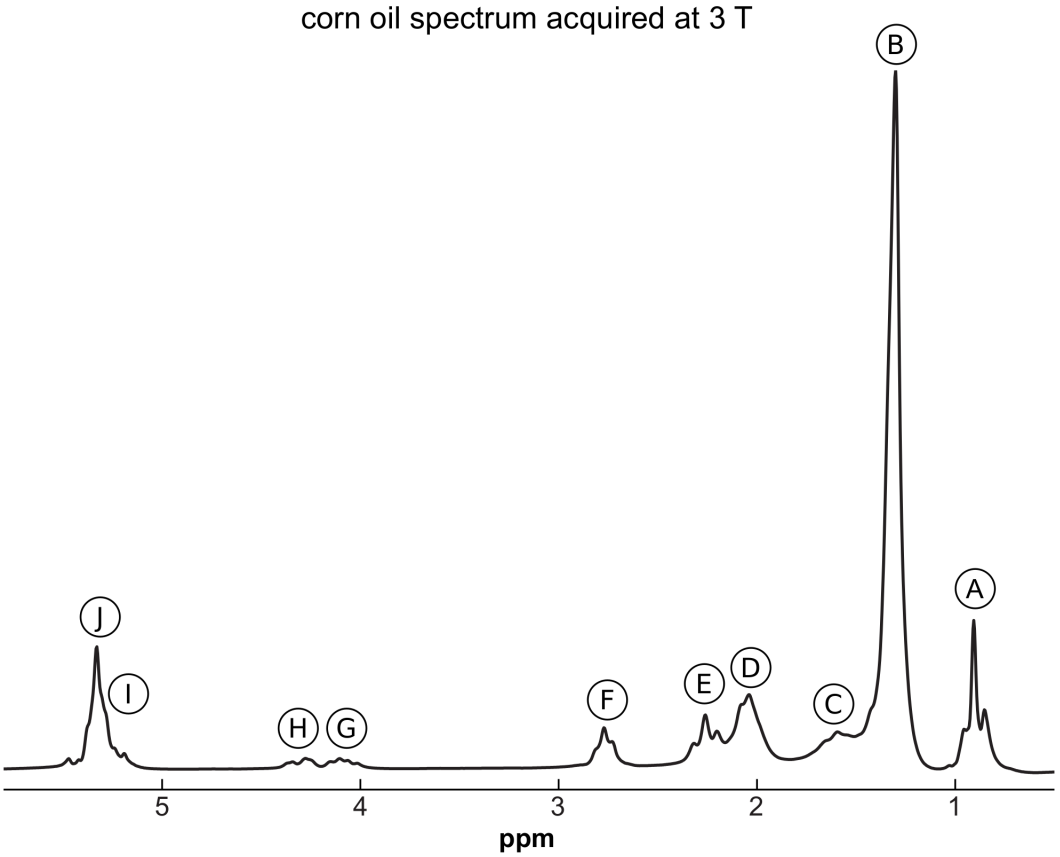


**Figure 3.2:** Example of a triglyceride spectrum (corn oil) acquired on clinical 3 T scanner. The spectral features labeled with circled letters (A-J) match the protons given in Figure 3.1.

Fat quantification in water–fat imaging uses a fixed triglyceride structure with usually a reduced number of frequency components modeled together with water (see also Section 5.2). For example, the six peak fat spectrum calibration for vertebral bone marrow [63] that was used in JP-III is given in Table 3.1. The corresponding relative amplitudes and relative frequency shifts to water at 3 T and at 37 °C were 0.0904, 0.6245, 0.1579, 0.0141, 0.0402 and 0.0729; and −485 Hz, −434 Hz, −332 Hz, −249 Hz, −51 Hz and 77 Hz, respectively. Please note, that the Larmor frequency of water shows a non-neglectable tempature dependence as compared to fat [64]. Therefore, the chemical shift difference between water and fat is also temperature dependent and has to be considered when e.g. phantom experiments at room temperature are conducted. Although it is rarely explicitly stated, most literature is assuming body temperature of 37 °C in the water–fat separation process. In cases where fat is simplified and treated as a single frequency in MRI literature, only the dominant methylene peak (B) at 1.30 ppm is modeled.

| peak | chemical shift (ppm) | type | relative amplitudes | relative amplitudes of used vertebral bone marrow model [63] |
|---|---|---|---|---|
| A | 0.90 | methyl | 9 | 9 |
| B | 1.30 | methylene | [(CL – 4) × 6] – (ndb × 8) + (nmidb × 2) | 56.16 |
| C | 1.60 | $\beta$-carboxyl | 6 | 6 |
| D | 2.02 | $\alpha$-olefinic | (ndb – nmidb) × 4 | 9.72 |
| E | 2.24 | $\alpha$-carboxyl | 6 | 6 |
| F | 2.75 | diallylic | nmidb × 2 | 1.4 |
| G | 4.10 | glycerol | 2 | 2 |
| H | 4.30 | glycerol | 2 | 2 |
| I | 5.19 | glycerol | 1 | 1 |
| J | 5.29 | olefinic | ndb × 2 | 6.26 |

**Table 3.1:** Triglyceride peak assignment and modeling in MR-based spectroscopy and imaging. Peaks A – J match the protons given in Figure 3.1. Relative amplitudes are also given for the vertebral bone marrow model with ndb = 3.13, nmidb = 0.7 and CL = 17.3 according to [63]. Summary based on [62, 63, 65–67].

# 4 Single-voxel Magnetic Resonance Spectroscopy

MRS is the direct translation of NMR spectroscopy into the clinical setting. Similar as in NMR, the main aspect of MRS is the differentiation of nuclei of a particular isotope based on their chemical shift.

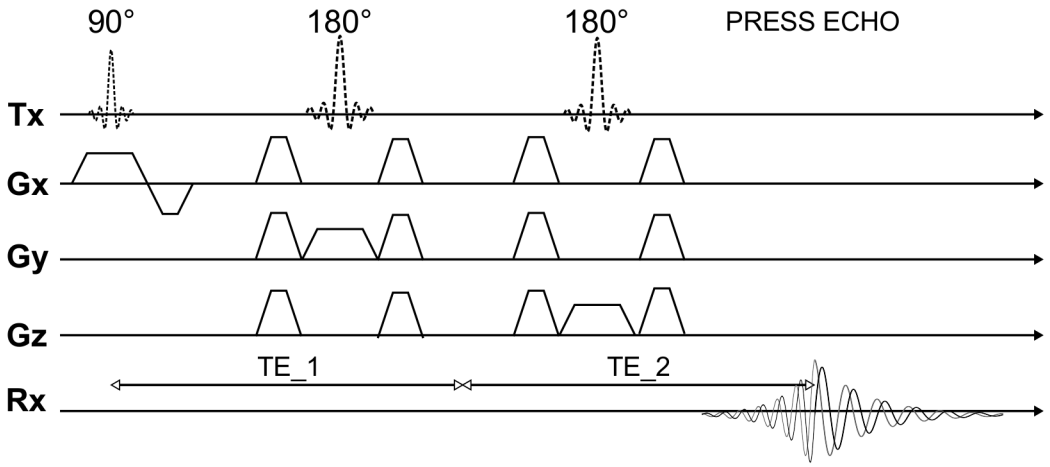


**Figure 4.1:** Single-voxel magnetic resonance spectroscopy sequence diagram: Point-resolved spectroscopy (PRESS). Total echo time TE is the sum of TE_1 and TE_2. The gray and black signal curves represent the real and imaginary component of the complex signal, respectively. Tx, transmission; Rx, reception; Gx, gradient in x-direction; Gy, gradient in y-direction; Gz, gradient in z-direction.

MRS usually employs a technique for localization as this is needed to probe a volume of interest (VOI) within an object. Single-voxel MRS refers to localization techniques to measure only signal within a VOI which is usually selected by the intersection of three perpendicular slice-selective excitations. The most frequently used single-voxel MRS techniques are point-resolved spectroscopy (PRESS) [68] and stimulated echo acquisition mode (STEAM) [69] as depicted in Figure 4.1 and Figure 4.2, respectively. A PRESS sequence consists of a 90° pulse followed by two refocusing 180° pulses forming a spin echo. The magnetization is kept in the transverse plane after the first 90° until its detection and is therefore only affected by $T_2$ relaxation. In contrast, a STEAM sequence uses three 90°pulses, produces a stimulated echo and is sensitive to both $T_1$ and $T_2$ relaxation as the magnetization is also stored in the longitudinal axis between the second and third RF pulse. PRESS has the advantage of a higher SNR compared to STEAM, but the 180° pulses also need more time to perform

and consequently the achievable TEs are longer compared to STEAM. Therefore STEAM is usually first choice when short $T_2$ species are of interest and good VOI selection needs to be achieved.

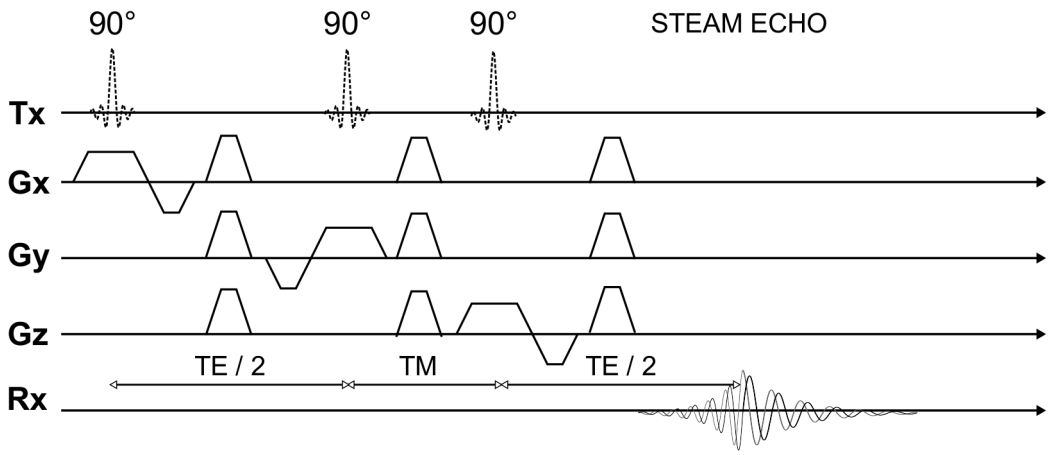


**Figure 4.2:** Single-voxel magnetic resonance spectroscopy sequence diagram: Stimulated echo acquisition mode (STEAM). The gray and black signal curves represent the real and imaginary component of the complex signal, respectively. TE, echo time; TM, mixing time; Tx, transmission; Rx, reception; Gx, gradient in x-direction; Gy, gradient in y-direction; Gz, gradient in z-direction.

## 4.1 Diffusion-weighted Stimulated Echo Acquisition Mode Spectroscopy (DW-STEAM)

Diffusion arising from e.g. Brownian motion of the molecules causes an attenuation of the measured signal, when a diffusion-weighting gradient is played out in a pulse sequence. The attenuation of the signal depends on the product of the diffusion coefficient $D$ (usually given in $\mathrm{mm\,s^{-2}}$) and a factor called b-value (in $\mathrm{s\,mm^{-1}}$). The resulting signal $S$ is exponentially weighted by the variance of the Gaussian phase distribution equal to the product $bD$:

$$S = S_0 e^{-bD} \tag{4.1}$$

where $S_0$ is the signal intensity of the non-weighted signal. Instead of the diffusion coefficient the apparent diffusion coefficient (ADC) is usually reported in MR to also acknowledge restriction effects [70].

In order to achieve diffusion weighting in a single-voxel STEAM MRS sequence [71], diffusion encoding gradients can be added after the first and third RF pulse when the magnetization is on the transverse plan. Figure 4.3 shows the diffusion-weighted STEAM (DW-STEAM) sequence scheme employed in JP-I, including non-motion-compensated diffusion encoding gradients ($m_1 \neq 0$ ) in each axis.

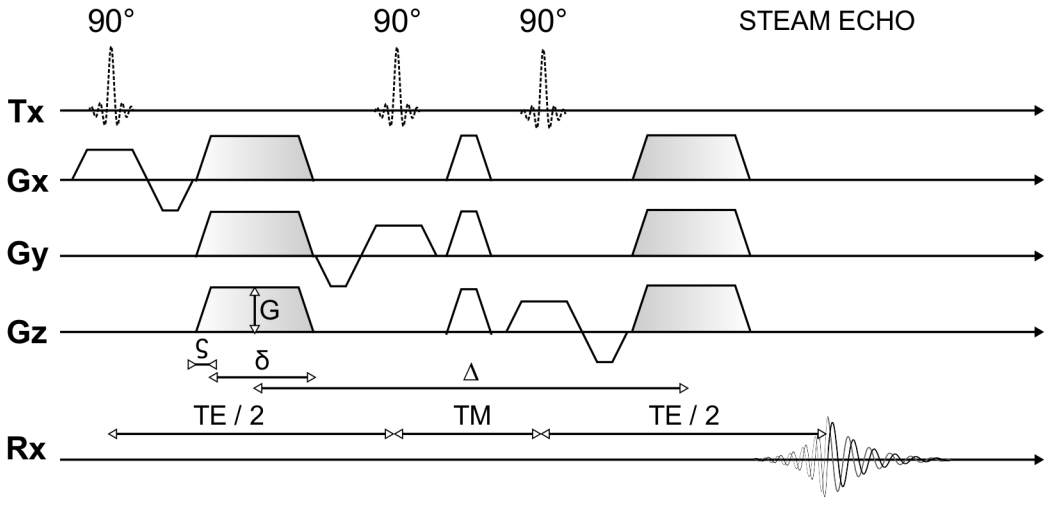


**Figure 4.3:** Single-voxel magnetic resonance spectroscopy sequence diagram: diffusion-weighted stimulated echo acquisition mode spectroscopy (DW-STEAM). Diffusion encoding gradients are filled out with a white to gray gradient. The gradient strength $G$, effective gradient duration $\delta$, diffusion time $\Delta$ and gradient ramp duration $\zeta$ can be used to estimate the b-value according to Equation (4.2). The gray and black signal curves represent the real and imaginary component of the complex signal, respectively. TE, echo time; TM, mixing time; Tx, transmission; Rx, reception; Gx, gradient in x-direction; Gy, gradient in y-direction; Gz, gradient in z-direction.

For the employed DW-STEAM sequence (Figure 4.3) with trapezoidal gradient waveforms [72], the b-value can be approximated by

$$b = \gamma^2 G^2 \left[\delta^2 \left(\Delta - \delta/3\right) + \zeta^3/30 - \delta\zeta^2/6\right] \tag{4.2}$$

where $G$ is the gradient strength, $\delta$ is the effective gradient duration (assuming rectangular gradients), $\Delta$ is the diffusion time which equals the duration between the center lobes of the two diffusion-weighting gradients and $\zeta$ is the duration of the gradient ramp.

# 5 Quantitative Chemical Shift Encoding-based Water–fat Imaging

In imaging, the focus switches from retrieving chemical shift information as compared with spectroscopy to spatial information. As described in Section 2.2.6, spatial encoding has to be applied in order to retain spatial information from the acquired signal during the reconstruction process, which has been very briefly described in Section 2.2.7. In quantitative chemical shift-based water–fat imaging often 3D SPGR sequences are employed due to their high SNR efficiency and relatively simple signal evolution. In the following the most important aspects of the employed 3D SPGR, including RF spoiling, steady state and the water–fat signal separation, are summarized.

## 5.1 3D Spoiled Gradient-echo Acquisition

SPGR sequences spoil the transverse magnetic coherences and thereby allow the acquisition of proton density or $T_1$-weighted images. The SPGR sequence used in the present studies uses time-interleaving of the acquired gradient echoes by splitting them in two TRs as shown in Figure 5.1. This allows to decouple the achievable imaging resolution from the echo time spacing.

### 5.1.1 Spoiling

Both gradient spoiling and RF spoiling were applied in the present work. For gradient spoiling, spoiler gradients with a certain strength are played out in the slice / slab selection and readout direction at the end of each TR before the next RF pulse to dephase the remaining magnetization. Using RF spoiling, by definition the phase of the applied RF pulse is incrementally changed by a phase increment in order to achieve optimal spoiling of transverse magnetization after each TR. This phase increment is typically set to 117° [73], since computer simulations have shown that for this particular phase increment the transverse magnetization prior to each RF pulse is neglectable over a wide range of flip angles, $T_1$ and $T_2$. RF spoiling mainly affects the way steady state is approached and its signal level [74]. Therefore RF spoiling only affects the magnitude signal and has no influence on the measured phase, as the receiver phase is by definition synchronized with the RF phase.

### 5.1.2 Approach to Steady State

In many applications, the SPGR sequence should have reached the steady state condition before the sampling of the k-space starts. Otherwise the function describing how steady state is approached will serve as a k-space filter.

In the following the number of required startup pulses or TRs using an arbitrary constant flip angle to achieve the steady state condition is derived similar to [75, p. 460]. According

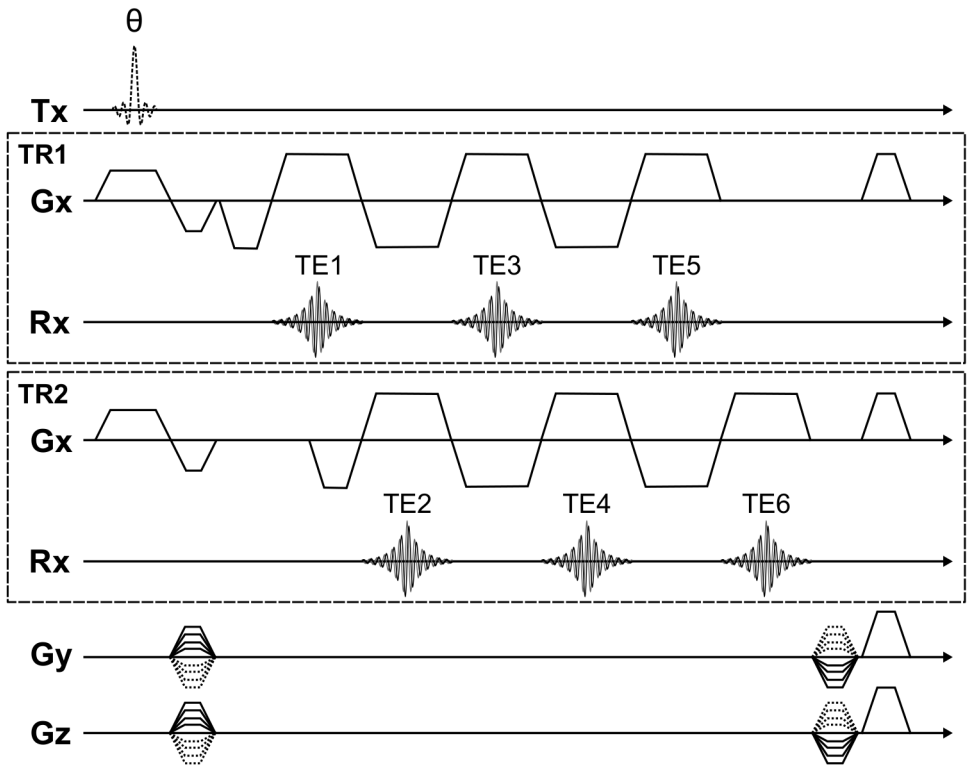


**Figure 5.1:** 3D spoiled gradient-echo sequence: A 3D time-interleaved multi-echo gradient-echo (TIMGRE) sequence with six echoes acquired in two interleaved TRs using monopolar readout gradients was used for quantitative chemical shift encoding-based water–fat imaging. The gray and black signal curves represent the real and imaginary component of the complex signal, respectively.

to [75, p. 460] the longitudinal magnetization $M_z^-(n,\theta)$ after the $n$th repetition applying a constant flip angle $\theta$ is given by

$$M_z^-(n,\theta) = M_0\left(1-e^{-\frac{TR}{T_1}}\right)\frac{\left(1-\left(\cos\theta e^{-\frac{TR}{T_1}}\right)^n\right)}{1-\cos\theta e^{-\frac{TR}{T_1}}} + M_0\left(\cos\theta e^{-\frac{TR}{T_1}}\right)^n \quad n \geq 1 \tag{5.1}$$

The steady state condition of (5.1) yields then

$$\lim_{n\to\infty} M_z^-(n,\theta) = M_{zss} = M_0\frac{\left(1-e^{-\frac{TR}{T_1}}\right)}{1-\cos\theta e^{-\frac{TR}{T_1}}} \tag{5.2}$$

The relative error estimating $M_z^-(n)$ by $M_z^-(\infty)$ at the $(n+1)^{st}$ pulse for an arbitrary angle $\theta$ can be defined as

$$\begin{aligned}\alpha &\equiv \frac{M_z^- (n,\theta) - M_{zss}(\theta)}{M_{zss}(\theta)} \\ &= \frac{(\cos(\theta) - 1)\left(e^{-\frac{TR}{T_1}}\cos(\theta)\right)^n}{1 - e^{\frac{TR}{T_1}}}\end{aligned} \tag{5.3}$$

Hence, the number of required pulses $n_\alpha$, which are needed to reach steady state with an arbitrary constant flip angle $\theta$ and maximum relative error $\alpha$ is then

$$n_\alpha = \text{ceil}\left\{\ln\left[\frac{\alpha\left(1 - e^{\frac{TR}{T_1}}\right)}{(\cos(\theta) - 1)}\right]\ln\left(e^{-\frac{TR}{T_1}}\cos(\theta)\right)^{-1}\right\} \tag{5.4}$$

where the ceil function denotes the next largest integer of the argument.

Equation (5.4) is plotted in Figure 5.2 for $\alpha = 0.01$, $\theta = 3°$, TR ranging from 5 ms to 20 ms and $T_1$ ranging from 250 ms to 1500 ms.

Equation (5.4) can also be simplified when the Ernst angle $\theta_E$ is used instead of an arbitrary constant flip angle $\theta$ [75, p. 461]:

$$n_{\alpha_E} = \text{ceil}\left[-\frac{T_1}{2TR}\ln(\alpha) - \frac{1}{2}\right] \tag{5.5}$$

## 5.2 Water–fat Signal Model

The acquired multi-echo data can then be used to estimate water, fat, $T_2^*$ and the underlying fieldmap. The complex formulation-based water–fat signal model, which is commonly used incorporates the complex spectral appearance of water and fat linked with a common relaxation rate $R_2^*$ for all spectral components, can be written as

$$S(t_n) = \left(W + F\sum_{m=1}^{M}\alpha_m e^{i2\pi\Delta f_m t_n}\right)e^{i2\pi f_B t_n}e^{-R_2^* t_n} \tag{5.6}$$

where $W$ and $F$ denote the complex water and fat signals, respectively; $R_2*$ denotes the real-valued apparent transverse relaxation rate; $f_B$ is the real-valued fieldmap; $t_n$ is the echo time of the $n$th echo; and $\alpha_p$ and $\Delta f_p$ refer to the $p$th (1,...,$P$) relative peak amplitude and frequency shift relative to water of the individual peaks of the employed fat model, respectively. The signal model (Equation (5.6)) itself assumes the absence of hardware imperfections and doesn't include e.g. physical spatial effects such as the concomitant gradient field. An example of how phase errors due to hardware imperfections and the concomitant gradient field can effect the resulting water–fat separation process is shown in the PDFF maps in Figure 5.3. The left and right image show PDFF maps without and with prior phase correction of confounding factors, respectively.

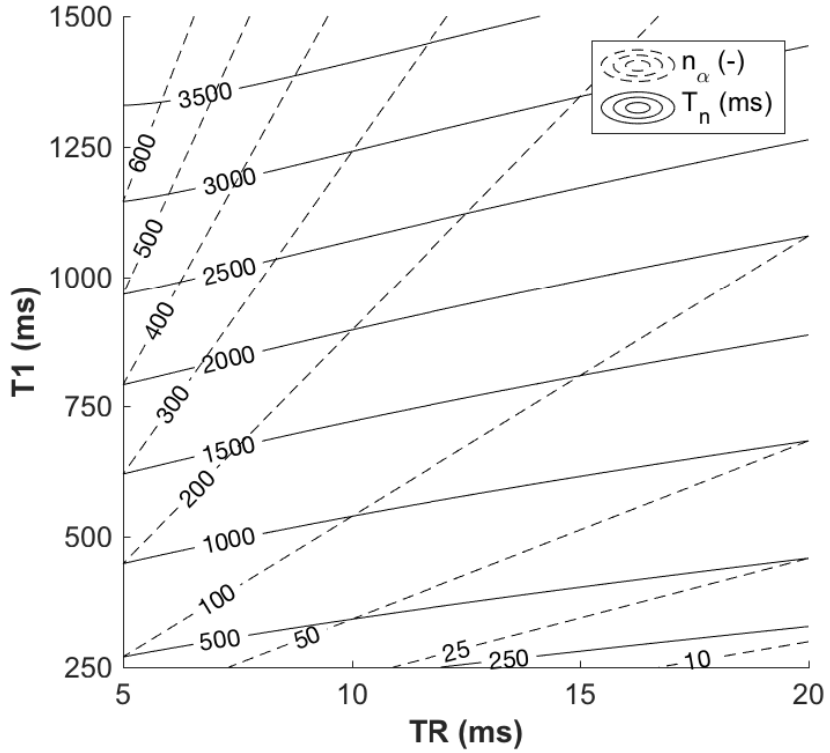


**Figure 5.2:** Contour plot showing the number of required startup pulses $n_\alpha$ (dashed contour) and total startup time $T_n$ (solid contour) needed to reach steady state according to Equation (5.4) for a given $\alpha$ of 0.01, flip angle $\theta$ of 3°, TR ranging from 5 ms to 20 ms and $T_1$ ranging from 250 ms to 1500 ms.

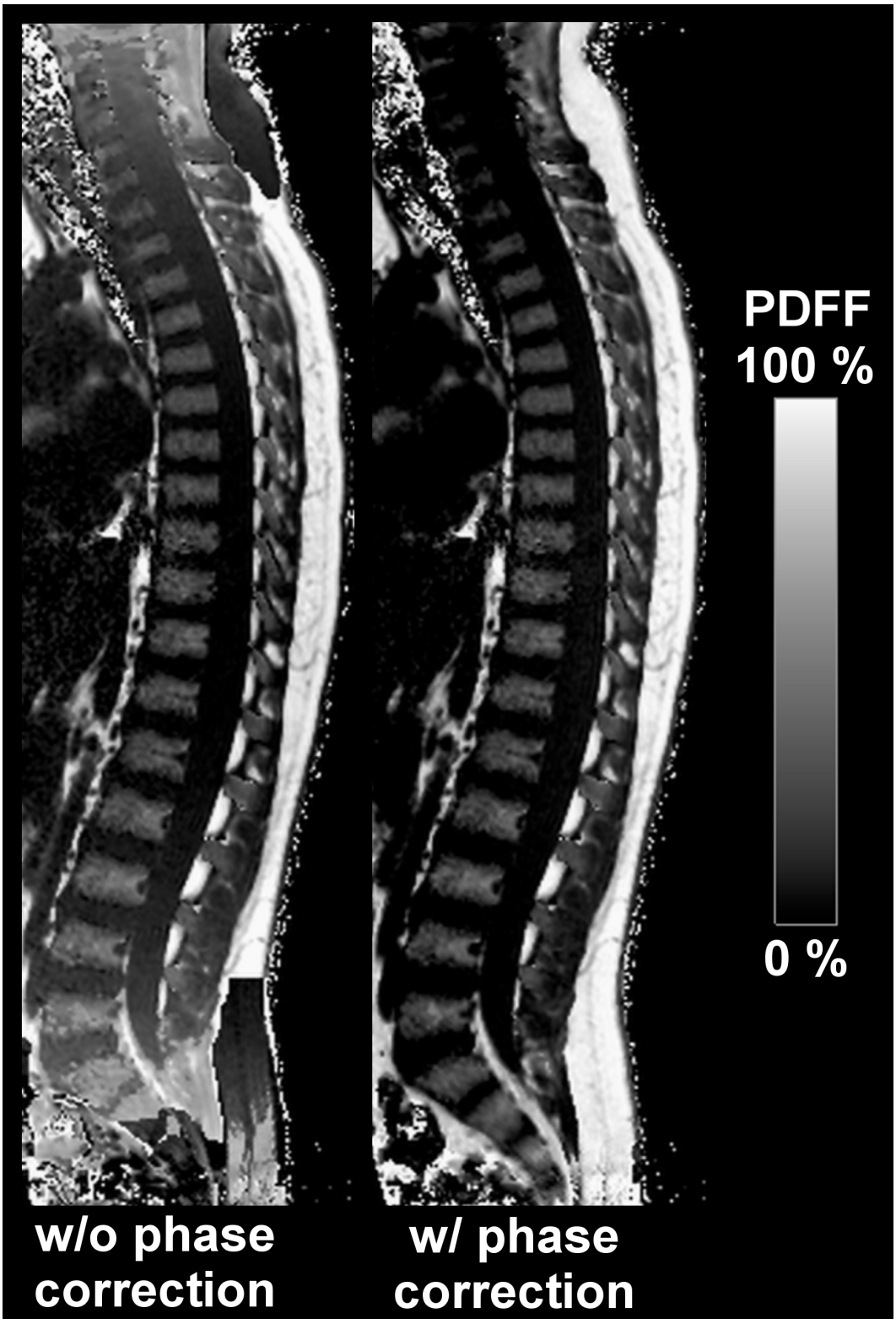


**Figure 5.3:** Representative full spine PDFF maps obtained in a 9-year-old male from JP-III without and with phase correction as described in JP-II, respectively. Note the increasing PDFF bias which is dominant in feet / head direction and the presence of water–fat-swaps towards the edges of the FOV without phase correction. PDFF, proton density fat fraction; FOV, field of view; w/, with; w/o, without.

# 6 Compliance with Ethical Standards

All investigations performed in studies involving human participants were in accordance with the ethical standards of the institutional and/or national research committee and with the 1964 Helsinki declaration and its later amendments or comparable ethical standards. Informed consent was obtained from all individual participants included in the studies. The study performed at Phoenix Children's Hospital was HIPAA-compliant (Health Insurance Portability and Accountability Act).

# 7 Comprising Journal Publications

## 7.1 Journal Publication I: Diffusion-Weighted Stimulated Echo Acquisition Mode (DW-STEAM) MR Spectroscopy to Measure Fat Unsaturation in Regions with Low Proton-Density Fat Fraction

The publication entitled *Diffusion-Weighted Stimulated Echo Acquisition Mode (DW-STEAM) MR Spectroscopy to Measure Fat Unsaturation in Regions with Low Proton-Density Fat Fraction* was published in Magnetic Resonance in Medicine (ISSN: 1522-2594). The manuscript was authored by Stefan Ruschke, Hermine Kienberger, Thomas Baum, Hendrik Kooijman, Marcus Settles, Axel Haase, Miachel Rychlik, Ernst J. Rummeny and Dimitrios C. Karampinos.

### 7.1.1 Abstract


#### Purpose

To propose and optimize diffusion-weighted stimulated echo acquisition mode (DW-STEAM) for measuring fat unsaturation in the presence of a strong water signal by suppressing the water signal based on a shorter $T_2$ and higher diffusivity of water relative to fat.

#### Methods

A parameter study for point-resolved spectroscopy (PRESS) and STEAM using oil phantoms was performed and correlated with gas chromatography (GC). Simulations of muscle tissue signal behavior using DW-STEAM and long–echo time (TE) PRESS and a parameter optimization for DW-STEAM were conducted. DW-STEAM and long-TE PRESS were applied in the gastrocnemius muscles of nine healthy subjects.

#### Results

STEAM with TE and mixing time (TM) up to 45 ms exhibited $R^2$ correlations above 0.98 with GC and little $T_2$-weighting and $J$-modulation for the quantified olefinic/methylene peak ratio. The optimal parameters for muscle tissue using DW-STEAM were b-value = 1800 s mm$^{-2}$, TE = 33 ms, TM = 30 ms, and TR = 2300 ms. In vivo measured mean olefinic signal-to-noise ratios were 72 and 40, mean apparent olefinic water fractions were 0.19 and 0.11 for DW-STEAM and long-TE PRESS, respectively.

#### Conclusion

Optimized DW-STEAM MR spectroscopy is superior to long-TE PRESS for measuring fat unsaturation, if a strong water peak prevents the olefinic fat signal's quantification at shorter TEs and water's tissue specific ADC is substantially higher than fat.

### 7.1.2 Author contributions

The first author performed the experiments (MR measurements); programmed the magnetic resonance pulse sequence (propriety hardware specific libraries and software from Philips Medical Systems (Best, The Netherlands)); implemented the reconstruction, post-processing and the quantification process using Matlab (Mathworks, Natick, MA). With the help and consultation form the coauthors; the first author designed the experiment; analyzed and interpreted the data; and wrote the paper.

## 7.2 Journal Publication II: Correction of phase errors in quantitative water–fat imaging using a monopolar time-interleaved multi-echo gradient echo sequence

The publication entitled *Correction of phase errors in quantitative water–fat imaging using a monopolar time-interleaved multi-echo gradient echo sequence* was published in Magnetic Resonance in Medicine (ISSN: 1522-2594). The manuscript was authored by Stefan Ruschke, Holger Eggers, Hendrik Kooijman, Maximilian N. Diefenbach, Thomas Baum, Axel Haase, Ernst J. Rummeny, Houchun H. Hu, and Dimitrios C. Karampinos.

### 7.2.1 Abstract

#### Purpose

To propose a phase error correction scheme for monopolar time-interleaved multi-echo gradient echo water–fat imaging that allows accurate and robust complex-based quantification of the proton density fat fraction (PDFF).

#### Methods

A three-step phase correction scheme is proposed to address a) a phase term induced by echo misalignments that can be measured with a reference scan using reversed readout polarity, b) a phase term induced by the concomitant gradient field that can be predicted from the gradient waveforms, and c) a phase offset between time-interleaved echo trains. Simulations were carried out to characterize the concomitant gradient field-induced PDFF bias and the performance estimating the phase offset between time-interleaved echo trains. Phantom experiments and in vivo liver and thigh imaging were performed to study the relevance of each of the three phase correction steps on PDFF accuracy and robustness.

#### Results

The simulation, phantom, and in vivo results showed in agreement with the theory an echo time-dependent PDFF bias introduced by the three phase error sources. The proposed phase correction scheme was found to provide accurate PDFF estimation independent of the employed echo time combination.

#### Conclusion

Complex-based time-interleaved water–fat imaging was found to give accurate and robust PDFF measurements after applying the proposed phase error correction scheme.

### 7.2.2 Author contributions

The first author performed the experiments (fabrication of MR phantoms, MR measurements); programmed the magnetic resonance pulse sequence (propriety hardware specific libraries and software from Philips Medical Systems (Best, The Netherlands)); implemented the reconstruction (Matlab (Mathworks, Natick, MA) using functionality provided by the propriety ReconFrame software (GyroTools, Zurich, Switzerland), post-processing and the quantification process. With the help and consultation form the coauthors; the first author designed the experiment; analyzed and interpreted the data; and wrote the manuscript.

## 7.3 Journal Publication III: Measurement of vertebral bone marrow proton density fat fraction in children using quantitative water–fat MRI

The publication entitled *Measurement of vertebral bone marrow proton density fat fraction in children using quantitative water–fat MRI* was published in Magnetic Resonance Materials in Physics, Biology and Medicine (ISSN: 1352-8661). The manuscript was authored by Stefan Ruschke, Amber Pokorney, Thomas Baum, Holger Eggers, Jeffrey H. Miller, Houchun H. Hu and Dimitrios C. Karampinos.

### 7.3.1 Abstract

#### Purpose

To investigate the feasibility of employing a 3D time-interleaved multi-echo gradient-echo (TIMGRE) sequence to measure the proton density fat fraction (PDFF) in the vertebral bone marrow (VBM) of children and to examine cross-sectional changes with age and intra-individual variations from the lumbar to the cervical region in the first two decades of life.

#### Methods

Quantitative water-fat imaging of the spine was performed in 93 patients (49 females; 44 males; age median 4.5 years; range: 0.1–17.6 years). For data acquisition, a six-echo 3D TIMGRE sequence was used with phase correction and complex-based water-fat separation. Additionally, single-voxel MR spectroscopy (MRS) was performed in the L4 vertebrae of 37 patients. VBM was manually segmented in the midsagittal slice of each vertebra. Univariable and multivariable linear regression models were calculated between averaged lumbar, thoracic and cervical bone marrow PDFF and age with an adjustment for sex, height, weight and body mass index percentile.

#### Results

Measured VBM PDFF correlated strongly between imaging and MRS ($R^2 = 0.92$, slope = 0.94, intercept = –0.72%). Lumbar, thoracic and cervical VBM PDFF correlated significantly

(all $p < 0.001$) with the natural logarithm of age. Differences between female and male patients were not significant ($p > 0.05$).

#### Conclusion

VBM development in children showed a sex-independent cross-sectional increase of PDFF correlating with the natural logarithm of age and an intra-individual decrease of PDFF from the lumbar to the cervical region in all age groups. The present results demonstrate the feasibility of using a 3D TIMGRE sequence for PDFF assessment in VBM of children.

### 7.3.2 Author contributions

The first author coordinated the study; programmed the magnetic resonance pulse sequence (using propriety hardware specific libraries and software from Philips Medical Systems (Best, The Netherlands)); implemented the reconstruction (Matlab (Mathworks, Natick, MA) using functionality provided by the propriety ReconFrame software (GyroTools, Zurich, Switzerland), post-processing and the quantification process; and performed the manual segmentation of the vertebral bone marrow compartment. With the help and consultation form the coauthors; the first author designed the experiment; analyzed and interpreted the data; and wrote the manuscript.

# 8 Discussion

The tremendous need for quantitative biomarkers to tackle clinical challenging diseases has been provoking the development of quantitative MR techniques and in particular quantitative water–fat MR over the last years. However, the application of quantitative MR methods in clinical practice remains limited and is still challenging.

## 8.1 Review of Existing Literature

The present work is based upon several preceding technical publications and studies in musculoskeletal tissues. The existing literature is separately reviewed for musculoskeletal single-voxel MRS with a focus on triglyceride characterization (Section 8.1.1), quantitative water–fat imaging (Section 8.1.2) and the assessment of vertebral bone marrow PDFF (Section 8.1.3) in the following:

### 8.1.1 Musculoskeletal Single-voxel Proton MRS

Single-voxel proton MRS is a pretty mature MR technique given that the first publication describing localized PRESS spectroscopy [68] and STEAM spectroscopy [69] both date back to 1987. The effect of diffusion is a well studied process using MR spectroscopy [76, 77]. The use of field gradients to encode diffusivity was first described in 1965 for spin echoes by Stejskal and Tanner [78] and in 1970 for stimulated echoes by Tanner [79], respectively. Subsequently, the combination of diffusion encoding gradients together with the acquisition of stimulated echoes was then first investigated in the context of imaging by Merboldt et al. [71] in 1985.

In musculoskeletal tissues, the water–fat ratio is dependent on the tissue type, anthropomorphic characeristics and can be also altered due to disease. Ideally, the MRS-based characterization of trigylcerides – espacially the degree of (un)saturation – is measured in the absence of any water signal at typical clinical field strengths of up to 3 T. Due to the minimal achievable linewidths in a clinical setting the water signal is overlapping with the olefinic signal arising from protons next to the double bounds in the fatty acid chains of triglycerides and therefore prevents the quantification of the olefinic signal. Methods that have routinely been used to suppress the water signal in 1D proton MRS include chemical shift–based water suppression (CHESS) [80], water suppression enhanced through T1 effects (WET) [81] and variable power RF pulses with optimized relaxation delays (VAPOR) [82]. However, the drawback of these techniques is that they potentially affect frequencies nearby the water peak and may therefore lead to a distortion of the olefinic lipid peak. Therefore, indirect methods for the characterization of the olefinic signal have also been proposed based on the quantification of the $\alpha$-olefinic and methyl signals [83] which are not confounded by the water signal. However, in some applications the achievable linewidth may be too broad and the measurement of these peaks may thus be challenging. Other approaches have been proposed that exploit differences in the MR detectable properties of water and fat. As for example, $T_2$ relaxation of water is usually much shorter compared to fat in most tissues. Long-TE MRS measurements have hence be proposed to reduce the water signal relative to the fat signal

[84, 85] albeit the reduced SNR. The effect of $J$-couplings becomes important in single-voxel MRS as a consequence of the prolonged TEs [86–89] . Based on the analysis of empirical data and comparison with gas chromatography PRESS with a TE of 200 ms [84, 90–92] and STEAM with a TE of 100 ms [92] were considered to be suitable for measuring the degree of triglyceride (un)saturation in the presence of the $J$-modulations. Again, the derived long TEs minimize the signal based on the $J$-modulation, but also significantly decrease the SNR.

Large differences in diffusivity between water and larger molecules [93, 94] were recently exploited in musculoskeletal MRS using diffusion-weighted spectroscopy, namely in the context of lipid characterization to differentiate between intramyocellular (IMCL) and extramyocellular lipids (EMCL) [95, 96], and to measure carbohydrate signal in the intervertebral discs [97]. Other studies on triglyceride (un)saturation in the muscle have been previously performed using also multi-dimensional single-voxel spectroscopy [98, 99] with the drawback of extensively prolonged scan times.

Due to the recent interest in triglyceride characterization in the musculoskeletal context [67], simplified parameters that can be measured in vivo using localized MRS have been proposed [8, 62]. Specifically, three popular parameters are used [62] that describe the number of double bonds per triglyceride (ndb), the number of methylene-interrupted double bonds per triglyceride (nmidb) and the mean fatty acid carbon chain length (CL). Especially the degree of (un)saturation of the fatty acid chains has been proposed as a useful biomarker in the context of osteoprosis [39, 44], obesity [100] and diabetes [42, 101, 102].

Recently there have been also efforts to map triglyceride characertistics using a model-based approach similar to chemical shift encoding-based water–fat imaging [66, 103, 104].

### 8.1.2 Quantitative Chemical Shift Encoding-based Water–fat Imaging

The idea of chemical shift encoding-based water–fat imaging goes back to 1984 when Thomas Dixon proposed a modified spin echo sequence [1] acquiring two echoes with shifted echo times resulting in images with the water and fat signal being in-phase and out-of-phase, respectively. These two images allowed to obtain water-only and fat-only images. Thus the fat fraction can then be defined as the ratio of the fat signal over the sum of the water and the fat signal. However, several confounding factors challenge the assessment of a quantitative fat fraction map using the chemical shift encoding-based approach and were addressed since then.

In pursuance of accurate quantitative PDFF measurements both physical confounding effects and hardware imperfections or measurement biases were addressed. On one side, several physical effects were identified such as $B_0$ homogeneities [105, 106], $T_2^*$ decay [107, 108], different $T_1$ relaxation between the water and triglyceride component [109, 110], the complexity of the triglyceride signal model [108, 111], susceptibility-induced resonance shifts [112] and temperature-induced resonance shifts of water [64]. On the other side, noise bias [109, 110] and hardware imperfection-related effects were addressed, namely the correction of phase errors [113–117]. Recently, at 3 T monopolar sequences have been primarily used in combination with a hybrid water–fat separation method combining complex- and magnitude-based fitting [115, 116, 118] to mitigate the phase error induced fat fraction bias of the complex-based method.

The concomitant gradient field has been first described as a confounding factor at low field strenghts [119] and then at higher field strenghs in the context of phase contrast angiography [46], echo planar imaging [120, 121] and spiral imaging [122]. The correction of concomitant gradient field induced phase accumulation has been recently also picked up in the context of chemical shift encoding-based imaging to also evaluate the influence on $T_2^*$ [123, 124] and $B_0$

mapping [123]. The dependence of the performance of the water–fat separation process on the chosen TE step has been first investigated for three-point Dixon using Cramér-Rao lower bounds [125] and then extended to multi-echo-based quantitative water–fat imaging [117].

### 8.1.3 MR-based Measurement of Vertebral Bone Marrow Fat-fraction

The interest in the non-invasive assessment of the vertebral bone marrow fat fraction arises from the traditional differentiation of two major bone marrow compartments based on their histogenesis: red and yellow bone marrow describe the predominance of hematopoietic and lipid rich tissue [126], respectively. Normal physiology of bone marrow is characterized by the successive conversion from hematopoietic to lipid rich bone marrow depending on age, sex and skeletal site [127–130]. Scheller et al. [131] recently proposed a differentiation of bone marrow types based on their intrinsically response to hematopoietic demands [132]: Regulated marrow adipose tissue (MAT) contains single interspersed adipocytes with active haematopoiesis as compared to constitutive MAT consisting of larger adipocytes with reduced haematopoiesis [133].

Both MR spectroscopy [63, 134–139] and imaging [137, 140–142] have been previously proposed to asses the presence of hematopoietic and lipid rich bone marrow by measuring vertebral bone marrow PDFF. Recent studies have also shown correlations between PDFF and bone marrow cellularity [143–145].

Existing studies assessing vertebral bone marrow PDFF have primarily focused on the adult population and hence only limited data is available in children. Particularly, the finding of bone marrow fat fraction being negatively associated with trabecular bone density [39, 41] has raised interest in the pathophysiological relationship between hemocytoblasts, osteoblasts, and adipocytes, as well as its implications for structural skeletal integrity [146]. Furthermore, a better understanding of bone development during childhood [18] may also help to gain insight into potential effects on adverse skeletal health throughout later life. Quantitative data on the bone marrow conversion process measuring PDFF has only been published employing MRS by Kugel et al. [147] and Griffith et al. [148] for age groups in the range from 11–95 years and 62–90 years, respectively. Significant higher bone marrow PDFF in males compared to females was reported in the age group of 31–40 years by Kugel et al. [147]. Griffith et al. [148] then found in accordance with an earlier non-quantitative study [149] a sharp increase of vertebral bone marrow PDFF in postemenopausal women which lead to a reversal of the significant difference in vertbral bone marrow PDFF. The PDFF increase in postmenopausal women was explained by changes in the body fat distribution [150–152] due to a declining estrogen level. It has been known that bone marrow consists of hematopoietic marrow only at birth [127] followed by the exponential accumulation of adipocytes at distal skelatal sites and relative slow conversion rate in the vertebral bone marrow [128, 129]. Previous studies using $T_1$-weighted MRI however already hinted at a more rapid increase of vertebral bone marrow fat fraction in the first years of life [153–156].

Vertebral bone marrow PDFF dependence on vertebral location has been previously investigated in spine segments in preliminary studies on the lumbar vertebrae [135] and the S2–T10 vertebrae [137]; and in an osteoporisis study for the L1–L4 vertebrae [157]. Only one previous study included an image-based full spine PDFF characterization in the adult population [141]. All the aforementioned studies on vertebral bone marrow PDFF dependence on vertebral location reported decreasing PDFF values from the lumbar vertebrae towards the cervical vertebrae.

## 8.2 Present Work

The present work includes several contributions to the field of musculoskeletal MR. JP-I describes a technique to characterize triglyceride (un)saturation in muscle tissue using diffusion-weighted magnetic resonance spectroscopy. JP-II emphasizes on robust water–fat quantification using spoiled gradient-echo-based magnetic resonance imaging. Finally, JP-III applies the technique presented in JP-II in bone marrow PDFF quantification in the pediatric spine to investigate bone marrow development in the first two decades of life.

### 8.2.1 Novelty

The three journal publications contribute to the field of musculoskeletal MR. Particularly, JP-I improves triglyceride characterization in muscle tissue and other tissues accompanying low PDFF content using MRS. The proposed diffusion-weighted MRS method has been shown to outperform a previously used spectroscopic method for triglyceride (un)saturation characterization in muscle tissue and is a promising candidate for the investigation of triglyceride (un)saturation patterns. Previously, triglyceride (un)saturation has been mainly characterized in subcutaneous and visceral adipose tissue.

JP-II pushes forward quantitative chemical-shift encoding-based water–fat imaging using a complex-based water–fat formulation. The proposed method builds the basis for robust and accurate PDFF quantification in clinical studies. The advantage of being able to decouple the achievable resolution from the performance of the water–fat decomposition will have a positive impact on future clinical studies allowing the combination of both — robust water–fat imaging at high resolution. The introduced correction of the concomitant gradient field induced phase variations enables also the imaging of large field of views which is helpful in clinical studies investigating e.g. body composition. Future developments in the field of water–fat MRI will also benefit from the gained deeper understanding of confounding factors in chemical-shift and gradient-echo-based water–fat imaging.

Finally, JP-III demonstrates the utility and feasibility of quantitative water–fat imaging in the pediatric spine measuring vertebral bone marrow PDFF. The sex-independent cross-sectional increase of PDFF strongly correlated with the natural logarithm of age and may serve as an initial guess for the normal vertebral bone marrow development throughout the first years of life. Additionally, an intra-individual decrease of PDFF from the lumbar to the cervical region with increasing slope and intercept from younger towards older subjects was observed for the first time.

### 8.2.2 Impact

The present work advances the field of quantitative water–fat magnetic resonance. The proposed technique described in JP-I allows the robust and noninvasive probing of triglyceride (un)saturation in tissues with low PDFF which is of high clinical interest. The accurate measurement of changes in triglyceride (un)saturation in tissues with low PDFF could be of high clinical relevance including applications in the liver [62, 158], heart [159], kidney [160, 161] and bone marrow [39, 44].

JP-II contributes to improved accuracy in measuring PDFF using quantitative chemical-shift encoding-based water–fat imaging, which is critical in the clinical context. For example, the PDFF cutoff level for hepatic triglyceride content suggesting the prevalence of hepatic steatosis was estimated to be of the order of 5% [162]. The improvement in accuracy and

robustness will be beneficial in multiple clinical applications including assessment of bone health [41, 43, 140, 163], metabolic disorders [2, 3, 164] and cancer [6, 7]. Additional potential applications include the post-therapeutic monitoring of bone marrow patterns after radiation and chemotherapy-based cancer treatments [165–168], the radiation therapy planning based on the quantitative distribution of active bone marrow [169] and as a complement to biopsy providing additional information to support the grading of hematologic malignancies [170].

The application of the technique described in JP-II was translated to a clinical setting given in JP-III. The technique was applied to measure PDFF in the pediatric spine and the results showed a sex-independent natural logarithmic increase of spinal bone marrow PDFF with age.

All developed methods can be used in the clinical setting and have been tested using standard clinical MRI hardware. The proposed methods are applied in currently running clinical studies. Already published subsequent and related work can be found in the listing of related publications.

### 8.2.3 Limitations

The application of DW-STEAM in musculoskeletal tissue to extract triglyceride (un)saturation revealed better SNR performance compared to long-TE PRESS as shown in JP-I. DW-STEAM is especially beneficial in tissues where the ADC of water is substantially higher compared to fat. The technique was optimized based on assumed tissue-specific ADC, $T_1$ and $T_2$ values for fat and water, where water was estimated to have a lower ADC and $T_2$ but higher $T_1$ compared to fat. Although these conditions should be satisfied in most musculoskeletal tissues, the approach may not be suitable to measure directly fat (un)saturation in e.g. vertebral bone marrow where the difference in ADC between water and fat is not sufficient and overall SNR is lower. The presence of both EMCL and IMCL in muscle tissue may inhibit the accurate extraction of a triglyceride (un)saturation level as these two compartments may not be separable using the proposed technique but the difference in $T_2$ and the disperse chemical shift may confound the quantification process. Another limitation is the potential presence of a broad water peak in the DW-STEAM measurement as it uses shorter TEs compared to the long-TE PRESS where signal from bound water should be completely decayed. This effect may cause a potential overestimation of the olefinic peak area and lead to an overestimation of the (un)saturation level. All simulations and the optimization included some simplifications that may affect the results in extreme cases. As for example a common $T_1$ and $T_2$ relaxation was assumed for all triglyceride frequencies. Although this a common assumption in clinical MR, the different relaxation properties between the methylene and the olefinic peak may lead to some systematic error. However, this effect is neglectable as long as TE and TM are kept as short as possible. Furthermore, $J$-coupling effects were not considered and only a mono-exponential signal decay was assumed. Nonetheless, this effect should be minimized in the employed TR and TM regime of up to 45 ms and therefore only cause minor errors.

The phase error correction scheme proposed in JP-II has also some limitations. The correction of the concomitant gradient field corrects only for lower order effects that are mainly arising from the slab selection and readout gradients. The concomitant gradient field caused by the phase encoding gradients has been neglected. Nevertheless, the approach achieved satisfying accuracy measuring PDFF in the analyzed scenarios. The phase offset between time-interleaved echo trains can be quite small and the performance of its estimation can be poor. Furthermore, to perform robust estimation of the phase offset between time-interleaved echo trains requires a minimum number of voxels with minimum requirements on SNR, low PDFF and moderate-to-low $R_2^*$. Therefore, the measured object requires to

have also qualifying regions and the scan has to be performed at a suitable resolution. These requirements may inhibit this technique from being applicable to e.g. 2D sequences as the number of suitable voxels that can be used for the estimation of the phase offset between time-interleaved echo trains may be insufficient. Furthermore, the phase offset between time-interleaved echo trains was only tested with two interleaved echo trains with three echoes each due to its frequent usage in various previous investigations. It may not be possible to directly apply the correction scheme in acquisition schemes with more then two interleaved echo trains. However, the echo misalignment and concomitant gradient field correction should be in general applicable to any TIMGRE-based acquisitions.

The study design for the measurement of vertebral bone marrow PDFF in children published in JP-III has some limitations. First, although the included cohort of 93 subjects had no pathological indications suggesting to have an impact on vertebral bone marrow PDFF, the examination of a healthy asymptomatic cohort of children would have been optimal to investigate normal vertebral bone marrow PDFF development. Second, the number of subjects with an age older than 9 years was limited and therefore, only a single group was formed with an age range from 9 to 18 years. Third, the performed manual segmentation of the vertebral bone marrow compartment in the medial slice assumes a homogeneous PDFF distribution throughout the bone marrow compartment which may not be an ideal assumption.

## 8.3 Perspectives

The perspectives of this work may include the application of the developed techniques in future clinical studies, as well as further technical developments and improvements building upon the proposed methods.

The diffusion-weighted single-voxel MRS sequence developed in JP-I is a versatile technique and can be used to explore many aspects of different tissues, such as probing unrestricted and restricted diffusion of water and fat. The developed acquisition, processing and quantification methods have built the foundation for an already ongoing research project on the in vivo measurement of restricted diffusion effects in fat aiming for the characterization of the mean adipocyte droplet size. Preliminary results on probing bone marrow adipocyte cell size using high b-value DW-STEAM at long diffusion times were recently presented by Weidlich et al. [171].

The work on monopolar TIMGRE sequences may serve as basis for future technical developments, e.g. replacement the monopolar readout with a more efficient bipolar readout. This may allow both high resolution and high SNR efficiency together with robust and accurate water–fat separation. The gained understanding of confounding factors in gradient-echo-based sequences will also help in translating the method to sequences using non-Cartesian k-space trajectories. The rigorous characterization and correction of phase altering effects will be essential for quantitative post-processing methods relying on accurate phase measurements, e.g. quantitative susceptibility mapping (QSM) in the presence of water and fat.

Finally, the reported correlations between vertebral bone marrow PDFF and age, as well as between spinal location and PDFF from JP-III may serve as basis for future studies relating bone marrow adiposity to bone health. For example, future prospective logitudinal studies could potentially investigate whether deviations form the strong correlations between vertebral bone marrow PDFF and age at young ages occur in subjects that have an increased osteoporotic fracture risk later in life. The potential gain in the understanding of the underlying mechanisms of osteoporosis may also have an impact on the current BMD-based clinical

routing which is used in the assessment of the individual osteoporotic fracture risk [35].

# Acknowledgments

I am grateful for all the support and thought-provoking impulses I have experienced during my time as a PhD student. First of all, I have to thank Dimitrios Karampinos for his exceptional and inspiring supervision. Furthermore I want to thank Ernst J. Rummeny and Axel Haase for their great support. Thomas Baum has been one of my main sources of clinical input during all the years – thank you for always explaining me the medical context. Marcus Settles and Carl Ganter, thank you for all the helpful discussions and input over the last years.

Being able to conduct part of the project at the Phoenix Children's Hospital completed this project. Dear Harry Hu, I thank you so much for giving me this great experience! I also want to thank Jeffrey Miller and Amber Pokorney for all the helpful insights.

Furthermore, I want to thank Hermine Kienberger and Michael Rychlik from the Chair of Analytical Food Chemistry for providing insights into gas chromatography and the support for the quantification of fatty acids in such great detail.

For all their tips and tricks, as well as their valuable support I would like to thank Hendrik Kooijman and Holger Eggers.

The stimulating atmosphere at work over the last years was incredible. Thanks to the entire research group: Barbara, Michael, Dominik, Max, Sarah, Sophia and Jan.

Last but not least I would also like to express my deepest thankfulness to my family, private and social shareholders, who were always loving and supportive!

# List of Symbols and Abbreviations

**Symbols**

| | |
|---|---|
| $\alpha$ | relative error [−] |
| $\alpha_p$ | relative amplitude of the to the $p$th fat peak [−] |
| $\Delta$ | diffusion time [s] |
| $\delta$ | effective gradient duration [s] |
| $\Delta B_i$ | local magnetic field inhomogeneity [Hz] |
| $\Delta f_p$ | relative frequency shift of the to the $p$th fat peak relative to water [Hz] |
| $\delta_{ppm}$ | chemical shift [ppm] |
| $\gamma$ | gyromagnetic ratio $\left[\mathrm{Hz\,T^{-1}}\right]$ |
| $\hbar$ | reduced Planck constant $\left[\mathrm{J\,s\,rad^{-1}}\right]$ |
| $\omega$ | precession frequency $\left[\mathrm{rad\,s^{-1}}\right]$ / [Hz] |
| $\omega_0$ | Larmor frequency $\left[\mathrm{rad\,s^{-1}}\right]$ |
| $\phi$ | phase angle [rad] |
| $\Phi_{cg}$ | concomitant field phase [rad] |
| $\rho$ | spin density $\left[\mathrm{m^{-3}}\right]$ |
| $\sigma$ | shielding constant [−] |
| $\tau$ | magnetic torque [N m] |
| $\theta$ | flip angle [°] / [rad] |
| $\theta_E$ | Ernst angle [rad] |
| $\boldsymbol{k}$ | k-space vector [cycles/m] |
| $\boldsymbol{r}$ | image space vector [m] |
| $\zeta$ | gradient ramp duration [s] |
| $A$ | intrinsic angular moment $\left[\mathrm{kg\,m^2\,s^{-1}}\right]$ |
| $B$ | magnetic field [T] |

| | |
|---|---|
| $b$ | b-value $\left[\mathrm{s\,m^{-2}}\right]$ |
| $B_0$ | static main magnetic field [T] |
| $B_1$ | radio frequency field [Hz] |
| $B_{cg}$ | concomitant gradient field to the lowest order [T] |
| $B_{eff}$ | effective static magnetic field considering shielding effects [T] |
| $D$ | diffusion coefficient $\left[\mathrm{m^2\,s^{-1}}\right]$ |
| $F$ | complex fat signal [−] |
| $f$ | resonance frequency [Hz] |
| $f_B$ | real valued field map [Hz] |
| $f_{ref}$ | reference frequency [Hz] |
| $G$ | gradient strength $\left[\mathrm{T\,m^{-1}}\right]$ |
| $G_x$ | magnetic gradient field along x dimension $\left[\mathrm{T\,m^{-1}}\right]$ |
| $G_y$ | magnetic gradient field along y dimension $\left[\mathrm{T\,m^{-1}}\right]$ |
| $G_z$ | magnetic gradient field along z dimension $\left[\mathrm{T\,m^{-1}}\right]$ |
| $k_B$ | Boltzmann constant $\left[\mathrm{J\,K^{-1}}\right]$ |
| $M$ | magnetic moment $\left[\mathrm{N\,m\,T^{-1}}\right]$ |
| $M_0$ | amplitude of the magnetization vector [−] |
| $m_1$ | first-order gradient moment $\left[\mathrm{T\,s^2\,m^{-1}}\right]$ |
| $M_x$ | spatial x component of the magnetization vector [−] |
| $M_y$ | spatial y component of the magnetization vector [−] |
| $M_z$ | spatial z component of the magnetization vector [−] |
| $n_\alpha$ | number of required startup pulses [−] |
| $R_2$ | transverse relaxation rate $\left[\mathrm{s^{-1}}\right]$ |
| $R_2'$ | reversible relaxation rate $\left[\mathrm{s^{-1}}\right]$ |
| $R_2^*$ | effective relaxation rate $\left[\mathrm{s^{-1}}\right]$ |
| $S_0$ | non-weighted signal intensity [−] |
| $T$ | temperature [K] |
| $t$ | time [s] |
| $T_1$ | spin-lattice (longitudinal) relaxation time [s] |

| | |
|---|---|
| $T_2$ | spin-spin (transverse) relaxation time [s] |
| $T_2'$ | reversible relaxation time [s] |
| $T_2^*$ | effective relaxation time [s] |
| $T_n$ | total startup time [s] |
| $T_{pe}$ | phase encoding time [s] |
| $W$ | complex water signal [−] |

**Abbreviations**

| | |
|---|---|
| 1D | one-dimensional |
| 2D | two-dimensional |
| 3D | three-dimensional |
| ADC | apparent diffusion coefficient |
| b-value | factor reflecting the strength and timing of diffusion weighting gradients |
| bSSFP | balanced steady state free precession |
| CL | mean fatty acid carbon chain length |
| CPMG | Carr-Purcell-Meiboom-Gill |
| CT | computed tomography |
| DFT | discrete Fourier transform |
| DW-STEAM | diffusion-weighted stimulated echo acquisition mode |
| EMCL | extramyocellular lipids |
| EPI | echo planar imaging |
| ESPRiT | efficient L1 iterative self-consistent parallel imaging |
| FID | free induction decay |
| FLASH | fast low angle shot |
| GRAPPA | generalized autocalibrating partially parallel acquisitions |
| GRASE | gradient and spin echo |
| IMCL | intramyocellular lipids |
| MR | magnetic resonance |
| MRF | magnetic resonance fingerprinting |
| MRI | magnetic resonance imaging |

| | |
|---|---|
| MRS | magnetic resonance spectroscopy |
| ndb | number of double bonds per triglyceride |
| nmidb | number of methylene-interrupted double bonds per triglyceride |
| NMR | nuclear magnetic resonance |
| PDFF | proton density fat fraction |
| PNS | peripheral nerve stimulation |
| PRESS | point-resolved spectroscopy |
| RARE | rapid acquisition with refocused echoes |
| RF pulse | radio frequency pulse |
| Rx | radio frequency reception |
| SAR | specific absorption rate |
| SE | spin echo |
| SENSE | sensitivity encoding |
| SMASH | simultaneous acquisition of spatial harmonics |
| SNR | signal-to-noise ratio |
| SPGR | spoiled gradient-echo |
| SSFP | steady state free precession |
| STE | stimulated echo |
| STEAM | stimulated echo acquisition mode |
| TE | echo time |
| TIMGRE | time-interleaved multi-echo gradient-echo |
| TM | mixing time |
| TMS | tetramethylsilane |
| TR | repetition time |
| Tx | radio frequency transmission |
| VOI | volume of interest |

# List of Figures

# List of Tables

# Bibliography


[1] W. T. Dixon, "Simple proton spectroscopic imaging.," *Radiology*, vol. 153, pp. 189–194, Oct. 1984.

[2] M. A. Bredella, C. M. Gill, A. V. Gerweck, M. G. Landa, V. Kumar, S. M. Daley, M. Torriani, and K. K. Miller, "Ectopic and serum lipid levels are positively associated with bone marrow fat in obesity.," *Radiology*, vol. 269, pp. 534–541, Nov. 2013.

[3] C. Cordes, M. Dieckmeyer, B. Ott, J. Shen, S. Ruschke, M. Settles, C. Eichhorn, J. S. Bauer, H. Kooijman, E. J. Rummeny, T. Skurk, T. Baum, H. Hauner, and D. C. Karampinos, "MR-detected changes in liver fat, abdominal fat, and vertebral bone marrow fat after a four-week calorie restriction in obese women," *Journal of Magnetic Resonance Imaging*, vol. 42, no. 5, pp. 1272–1280, 2015.

[4] T. Y. Kim and A. L. Schafer, "Diabetes and Bone Marrow Adiposity," *Current Osteoporosis Reports*, vol. 14, pp. 337–344, Oct. 2016.

[5] T. Yokoo, M. Shiehmorteza, G. Hamilton, T. Wolfson, M. E. Schroeder, M. S. Middleton, M. Bydder, A. C. Gamst, Y. Kono, A. Kuo, H. M. Patton, S. Horgan, J. E. Lavine, J. B. Schwimmer, and C. B. Sirlin, "Estimation of hepatic proton-density fat fraction by using MR imaging at 3.0 T.," *Radiology*, vol. 258, pp. 749–759, Mar. 2011.

[6] Y. P. Kim, S. Kannengiesser, M.-Y. Paek, S. Kim, T.-S. Chung, Y. H. Yoo, C.-S. Yoon, H.-T. Song, Y. H. Lee, and J.-S. Suh, "Differentiation between focal malignant marrow-replacing lesions and benign red marrow deposition of the spine with T2*-corrected fat-signal fraction map using a three-echo volume interpolated breath-hold gradient echo Dixon sequence.," *Korean Journal of Radiology*, vol. 15, pp. 781–791, Nov. 2014.

[7] C. Schraml, M. Schmid, S. Gatidis, H. Schmidt, C. la Fougère, K. Nikolaou, and N. F. Schwenzer, "Multiparametric analysis of bone marrow in cancer patients using simultaneous PET/MR imaging: Correlation of fat fraction, diffusivity, metabolic activity, and anthropometric data.," *Journal of Magnetic Resonance Imaging*, vol. 42, pp. 1048–1056, Oct. 2015.

[8] J. Ren, I. Dimitrov, A. D. Sherry, and C. R. Malloy, "Composition of adipose tissue and marrow fat in humans by 1H NMR at 7 Tesla.," *Journal of Lipid Research*, vol. 49, pp. 2055–2062, Sept. 2008.

[9] J. S. Flier, "The adipocyte: storage depot or node on the energy information superhighway?," *Cell*, vol. 80, pp. 15–18, Jan. 1995.

[10] K. Athenstaedt and G. Daum, "The life cycle of neutral lipids: Synthesis, storage and degradation," *Cellular and Molecular Life Sciences*, vol. 63, pp. 1355–1369, June 2006.

[11] S. M. Grundy, H. B. Brewer, J. I. Cleeman, S. C. Smith, C. Lenfant, and f. t. C. Participants, "Definition of Metabolic Syndrome: Report of the National Heart, Lung, and Blood Institute/American Heart Association Conference on Scientific Issues Related to Definition," *Circulation*, vol. 109, pp. 433–438, Jan. 2004.

[12] R. H. Eckel, S. M. Grundy, and P. Z. Zimmet, "The metabolic syndrome," *The Lancet*, vol. 365, pp. 1415–1428, Apr. 2005.

[13] L. Hutley and J. B. Prins, "Fat as an Endocrine Organ: Relationship to the Metabolic Syndrome," *The American Journal of the Medical Sciences*, vol. 330, pp. 280–289, Dec. 2005.

[14] D. Schellinger, C. S. Lin, J. Lim, H. G. Hatipoglu, J. C. Pezzullo, and A. J. Singer, "Bone marrow fat and bone mineral density on proton MR spectroscopy and dual-energy X-ray absorptiometry: their ratio as a new indicator of bone weakening.," *American Journal of Roentgenology*, vol. 183, pp. 1761–1765, Dec. 2004.

[15] C. J. Rosen and M. L. Bouxsein, "Mechanisms of Disease: is osteoporosis the obesity of bone?," *Nature Clinical Practice Rheumatology*, vol. 2, pp. 35–43, Jan. 2006.

[16] W. Shen, J. Chen, M. Punyanitya, S. Shapses, S. Heshka, and S. B. Heymsfield, "MRI-measured bone marrow adipose tissue is inversely related to DXA-measured bone mineral in Caucasian women.," *Osteoporosis International*, vol. 18, pp. 641–647, May 2007.

[17] M. J. Devlin, A. M. Cloutier, N. A. Thomas, D. A. Panus, S. Lotinun, I. Pinz, R. Baron, C. J. Rosen, and M. L. Bouxsein, "Caloric restriction leads to high marrow adiposity and low bone mass in growing mice.," *Journal of Bone and Mineral Research*, vol. 25, pp. 2078–2088, Sept. 2010.

[18] P. K. Fazeli, M. C. Horowitz, O. A. MacDougald, E. L. Scheller, M. S. Rodeheffer, C. J. Rosen, and A. Klibanski, "Marrow fat and bone–new perspectives.," *Journal of Clinical Endocrinology and Metabolism*, vol. 98, pp. 935–945, Mar. 2013.

[19] A. V. Schwartz, S. Sigurdsson, T. F. Hue, T. F. Lang, T. B. Harris, C. J. Rosen, E. Vittinghoff, K. Siggeirsdottir, G. Sigurdsson, D. Oskarsdottir, K. Shet, L. Palermo, V. Gudnason, and X. Li, "Vertebral bone marrow fat associated with lower trabecular BMD and prevalent vertebral fracture in older adults.," *Journal of Clinical Endocrinology and Metabolism*, vol. 98, pp. 2294–2300, June 2013.

[20] J. Kaur, "A Comprehensive Review on Metabolic Syndrome," *Cardiology Research and Practice*, vol. 2014, pp. 1–21, Mar. 2014.

[21] J. M. Dekker, C. Girman, T. Rhodes, G. Nijpels, C. D. A. Stehouwer, L. M. Bouter, and R. J. Heine, "Metabolic syndrome and 10-year cardiovascular disease risk in the Hoorn Study.," *Circulation*, vol. 112, pp. 666–673, Aug. 2005.

[22] K. G. M. M. Alberti, R. H. Eckel, S. M. Grundy, P. Z. Zimmet, J. I. Cleeman, K. A. Donato, J.-C. Fruchart, W. P. T. James, C. M. Loria, S. C. Smith, International Diabetes Federation Task Force on Epidemiology and Prevention, Hational Heart, Lung, and Blood Institute, American Heart Association, World Heart Federation, International Atherosclerosis Society, and International Association for the Study of

Obesity, "Harmonizing the metabolic syndrome: a joint interim statement of the International Diabetes Federation Task Force on Epidemiology and Prevention; National Heart, Lung, and Blood Institute; American Heart Association; World Heart Federation; International Atherosclerosis Society; and International Association for the Study of Obesity.," *Circulation*, vol. 120, pp. 1640–1645, Oct. 2009.

[23] N. T. Artinian, G. F. Fletcher, D. Mozaffarian, P. Kris-Etherton, L. Van Horn, A. H. Lichtenstein, S. Kumanyika, W. E. Kraus, J. L. Fleg, N. S. Redeker, J. C. Meininger, J. Banks, E. M. Stuart-Shor, B. J. Fletcher, T. D. Miller, S. Hughes, L. T. Braun, L. A. Kopin, K. Berra, L. L. Hayman, L. J. Ewing, P. A. Ades, J. L. Durstine, N. Houston-Miller, L. E. Burke, and American Heart Association Prevention Committee of the Council on Cardiovascular Nursing, "Interventions to promote physical activity and dietary lifestyle changes for cardiovascular risk factor reduction in adults: a scientific statement from the American Heart Association.," *Circulation*, vol. 122, pp. 406–441, July 2010.

[24] R. H. Eckel, S. E. Kahn, E. Ferrannini, A. B. Goldfine, D. M. Nathan, M. W. Schwartz, R. J. Smith, and S. R. Smith, "Obesity and type 2 diabetes: What can be unified and what needs to be individualized?," *Journal of Clinical Endocrinology and Metabolism*, vol. 96, pp. 1654–1663, June 2011.

[25] A. G. Bonomi and K. R. Westerterp, "Advances in physical activity monitoring and lifestyle interventions in obesity: a review.," *International Journal of Obesity*, vol. 36, pp. 167–177, Feb. 2012.

[26] H. Glauber and E. Karnieli, "Preventing type 2 diabetes mellitus: a call for personalized intervention.," *The Permanente Journal*, vol. 17, no. 3, pp. 74–79, 2013.

[27] K. N. Frayn, "Visceral fat and insulin resistance — causative or correlative?," *British Journal of Nutrition*, vol. 83, pp. S71–S77, June 2000.

[28] J. Machann, C. Thamer, N. Stefan, N. F. Schwenzer, K. Kantartzis, H.-U. Häring, C. D. Claussen, A. Fritsche, and F. Schick, "Follow-up whole-body assessment of adipose tissue compartments during a lifestyle intervention in a large cohort at increased risk for type 2 diabetes.," *Radiology*, vol. 257, pp. 353–363, Nov. 2010.

[29] G. Marchesini, M. Brizi, A. M. Morselli-Labate, G. Bianchi, E. Bugianesi, A. J. McCullough, G. Forlani, and N. Melchionda, "Association of nonalcoholic fatty liver disease with insulin resistance," *The American Journal of Medicine*, vol. 107, pp. 450–455, Nov. 1999.

[30] S. B. Reeder, I. Cruite, G. Hamilton, and C. B. Sirlin, "Quantitative assessment of liver fat with magnetic resonance imaging and spectroscopy.," *Journal of Magnetic Resonance Imaging*, vol. 34, pp. 729–749, Oct. 2011.

[31] A. Klibanski, L. Adams-Campbell, T. Bassford, S. N. Blair, S. D. Boden, K. Dickersin, D. R. Gifford, L. Glasse, S. R. Goldring, K. Hruska, S. R. Johnson, L. K. McCauley, W. E. Russell, and N. C. D. P. Osteopor, "Osteoporosis prevention, diagnosis, and therapy," *Journal of the American Medical Association*, vol. 285, no. 6, pp. 785–795, 2001.

[32] S. Boonen, P. Autier, M. Barette, D. Vanderschueren, P. Lips, and P. Haentjens, "Functional outcome and quality of life following hip fracture in elderly women: a prospective controlled study.," *Osteoporosis International*, vol. 15, pp. 87–94, Feb. 2004.

[33] T. Jalava, S. Sarna, L. Pylkkänen, B. Mawer, J. A. Kanis, P. Selby, M. Davies, J. Adams, R. M. Francis, J. Robinson, and E. McCloskey, "Association between vertebral fracture and increased mortality in osteoporotic patients.," *Journal of Bone and Mineral Research*, vol. 18, pp. 1254–1260, July 2003.

[34] F. Bleibler, A. Konnopka, P. Benzinger, K. Rapp, and H. H. König, "The health burden and costs of incident fractures attributable to osteoporosis from 2010 to 2050 in Germany—a demographic simulation model," *Osteoporosis International*, vol. 24, no. 3, pp. 835–847, 2013.

[35] S. C. E. Schuit, M. van der Klift, A. E. A. M. Weel, C. E. D. H. de Laet, H. Burger, E. Seeman, A. Hofman, A. G. Uitterlinden, J. P. T. M. van Leeuwen, and H. A. P. Pols, "Fracture incidence and association with bone mineral density in elderly men and women: The Rotterdam Study," *Bone*, vol. 34, pp. 195–202, Jan. 2004.

[36] E. S. Siris, Y.-T. Chen, T. A. Abbott, E. Barrett-Connor, P. D. Miller, L. E. Wehren, and M. L. Berger, "Bone Mineral Density Thresholds for Pharmacological Intervention to Prevent Fractures," *Archives of Internal Medicine*, vol. 164, pp. 1108–1112, May 2004.

[37] M. Janghorbani, R. M. Van Dam, W. C. Willett, and F. B. Hu, "Systematic Review of Type 1 and Type 2 Diabetes Mellitus and Risk of Fracture," *American Journal of Epidemiology*, vol. 166, pp. 495–505, Sept. 2007.

[38] J. A. Kanis, F. Borgstrom, C. De Laet, H. Johansson, O. Johnell, B. Jönsson, A. Oden, N. Zethraeus, B. Pfleger, and N. Khaltaev, "Assessment of fracture risk.," *Osteoporosis International*, vol. 16, pp. 581–589, June 2005.

[39] D. K. W. Yeung, J. F. Griffith, G. E. Antonio, F. K. H. Lee, J. Woo, and P. C. Leung, "Osteoporosis is associated with increased marrow fat content and decreased marrow fat unsaturation: a proton MR spectroscopy study.," *Journal of Magnetic Resonance Imaging*, vol. 22, p. 285, Aug. 2005.

[40] J. F. Griffith, D. K. W. Yeung, G. E. Antonio, F. K. H. Lee, A. W. L. Hong, S. Y. S. Wong, E. M. C. Lau, and P. C. Leung, "Vertebral bone mineral density, marrow perfusion, and fat content in healthy men and men with osteoporosis: dynamic contrast-enhanced MR imaging and MR spectroscopy.," *Radiology*, vol. 236, pp. 945–951, Sept. 2005.

[41] J. F. Griffith, D. K. W. Yeung, G. E. Antonio, S. Y. S. Wong, T. C. Y. Kwok, J. Woo, and P. C. Leung, "Vertebral marrow fat content and diffusion and perfusion indexes in women with varying bone density: MR evaluation.," *Radiology*, vol. 241, pp. 831–838, Dec. 2006.

[42] T. Baum, S. P. Yap, D. C. Karampinos, L. Nardo, D. Kuo, A. J. Burghardt, U. B. Masharani, A. V. Schwartz, X. Li, and T. M. Link, "Does vertebral bone marrow fat content correlate with abdominal adipose tissue, lumbar spine bone mineral density, and blood biomarkers in women with type 2 diabetes mellitus?," *Journal of Magnetic Resonance Imaging*, vol. 35, pp. 117–124, Jan. 2012.

[43] D. Schellinger, C. S. Lin, H. G. Hatipoglu, and D. Fertikh, "Potential value of vertebral proton MR spectroscopy in determining bone weakness.," *American Journal of Neuroradiology*, vol. 22, pp. 1620–1627, Sept. 2001.

[44] J. M. Patsch, X. Li, T. Baum, S. P. Yap, D. C. Karampinos, A. V. Schwartz, and T. M. Link, "Bone marrow fat composition as a novel imaging biomarker in postmenopausal women with prevalent fragility fractures.," *Journal of Bone and Mineral Research*, vol. 28, pp. 1721–1728, Aug. 2013.

[45] L. G. Hanson, "Is quantum mechanics necessary for understanding magnetic resonance?," *Concepts in Magnetic Resonance Part A*, vol. 32A, pp. 329–340, Sept. 2008.

[46] M. A. Bernstein, X. J. Zhou, J. A. Polzin, K. F. King, A. Ganin, N. J. Pelc, and G. H. Glover, "Concomitant gradient terms in phase contrast MR: Analysis and correction," *Magnetic Resonance in Medicine*, vol. 39, no. 2, pp. 300–308, 1998.

[47] J. Frahm, K. D. Merboldt, W. Hanicke, and A. Haase, "Stimulated echo imaging," *Journal of Magnetic Resonance*, vol. 64, pp. 81–93, Aug. 1985.

[48] H. Y. Carr, "Steady-State Free Precession in Nuclear Magnetic Resonance," *Physical Review*, vol. 112, pp. 1693–1701, Dec. 1958.

[49] D. Ma, V. Gulani, N. Seiberlich, K. Liu, J. L. Sunshine, J. L. Duerk, and M. A. Griswold, "Magnetic resonance fingerprinting.," *Nature*, vol. 495, pp. 187–192, Mar. 2013.

[50] H. Y. Carr and E. M. Purcell, "Effects of Diffusion on Free Precession in Nuclear Magnetic Resonance Experiments," *Physical Review*, vol. 94, pp. 630–638, May 1954.

[51] S. Meiboom and D. Gill, "Modified spin-echo method for measuring nuclear relaxation times," *Review of Scientific Instruments*, vol. 29, pp. 688–691, Dec. 1958.

[52] J. Hennig, A. Nauerth, and H. Friedburg, "RARE imaging: A fast imaging method for clinical MR," *Magnetic Resonance in Medicine*, vol. 3, pp. 823–833, Dec. 1986.

[53] K. Oshio and D. A. Feinberg, "GRASE (Gradient-and Spin-Echo) imaging: A novel fast MRI technique," *Magnetic Resonance in Medicine*, vol. 20, pp. 344–349, Aug. 1991.

[54] A. Haase, J. Frahm, D. Matthaei, W. Hanicke, and K. D. Merboldt, "FLASH imaging. Rapid NMR imaging using low flip-angle pulses," *Journal of Magnetic Resonance*, vol. 67, pp. 258–266, Apr. 1986.

[55] P. Irarrazabal and D. G. Nishimura, "Fast Three Dimensional Magnetic Resonance Imaging," *Magnetic Resonance in Medicine*, vol. 33, pp. 656–662, May 1995.

[56] D. K. Sodickson and W. J. Manning, "Simultaneous acquisition of spatial harmonics (SMASH): Fast imaging with radiofrequency coil arrays," *Magnetic Resonance in Medicine*, vol. 38, pp. 591–603, Oct. 1997.

[57] K. P. Pruessmann, M. Weiger, M. B. Scheidegger, and P. Boesiger, "SENSE: sensitivity encoding for fast MRI.," *Magnetic Resonance in Medicine*, vol. 42, pp. 952–962, Nov. 1999.

[58] M. A. Griswold, P. M. Jakob, R. M. Heidemann, M. Nittka, V. Jellus, J. Wang, B. Kiefer, and A. Haase, "Generalized autocalibrating partially parallel acquisitions (GRAPPA).," *Magnetic Resonance in Medicine*, vol. 47, pp. 1202–1210, June 2002.

[59] M. Uecker, P. Lai, M. J. Murphy, P. Virtue, M. Elad, J. M. Pauly, S. S. Vasanawala, and M. Lustig, "ESPIRiT–an eigenvalue approach to autocalibrating parallel MRI: where SENSE meets GRAPPA.," *Magnetic Resonance in Medicine*, vol. 71, pp. 990–1001, Mar. 2014.

[60] D. L. Donoho, "Compressed sensing," *IEEE Transactions on Information Theory*, vol. 52, no. 4, pp. 1289–1306.

[61] M. Lustig, D. Donoho, and J. M. Pauly, "Sparse MRI: The application of compressed sensing for rapid MR imaging," *Magnetic Resonance in Medicine*, vol. 58, pp. 1182–1195, Dec. 2007.

[62] G. Hamilton, G. Hamilton, T. Yokoo, T. Yokoo, M. Bydder, M. Bydder, I. Cruite, I. Cruite, M. E. Schroeder, M. E. Schroeder, C. B. Sirlin, C. B. Sirlin, M. S. Middleton, and M. S. Middleton, "In vivo characterization of the liver fat $^{1}$H MR spectrum.," *NMR in Biomedicine*, vol. 24, pp. 784–790, Aug. 2011.

[63] M. Dieckmeyer, S. Ruschke, C. Cordes, S. P. Yap, H. Kooijman, H. Hauner, E. J. Rummeny, J. S. Bauer, T. Baum, and D. C. Karampinos, "The need for T2 correction on MRS-based vertebral bone marrow fat quantification: implications for bone marrow fat fraction age dependence," *NMR in Biomedicine*, vol. 28, pp. 432–439, Apr. 2015.

[64] D. Hernando, S. D. Sharma, H. Kramer, and S. B. Reeder, "On the confounding effect of temperature on chemical shift-encoded fat quantification.," *Magnetic Resonance in Medicine*, vol. 72, pp. 464–470, Aug. 2014.

[65] G. Vlahov, "Application of NMR to the study of olive oils," *Progress in Nuclear Magnetic Resonance Spectroscopy*, vol. 35, pp. 341–357, Dec. 1999.

[66] J. Berglund, H. Ahlström, and J. Kullberg, "Model-based mapping of fat unsaturation and chain length by chemical shift imaging-phantom validation and in vivo feasibility," *Magnetic Resonance in Medicine*, vol. 68, pp. 1815–1827, Feb. 2012.

[67] G. Hamilton, A. N. Schlein, M. S. Middleton, C. A. Hooker, T. Wolfson, A. C. Gamst, R. Loomba, and C. B. Sirlin, "In vivo triglyceride composition of abdominal adipose tissue measured by $^{1}$H MRS at 3T," *Journal of Magnetic Resonance Imaging*, vol. 45, pp. 1455–1463, May 2017.

[68] P. A. Bottomley, "Spatial Localization in NMR Spectroscopy in Vivo," *Annals of the New York Academy of Sciences*, vol. 508, pp. 333–348, Nov. 1987.

[69] J. Frahm, K. D. Merboldt, and W. Hanicke, "Localized proton spectroscopy using stimulated echoes," *Journal of Magnetic Resonance*, vol. 72, pp. 502–508, May 1987.

[70] D. Le Bihan, E. Breton, D. Lallemand, P. Grenier, E. Cabanis, and M. Laval-Jeantet, "MR imaging of intravoxel incoherent motions: application to diffusion and perfusion in neurologic disorders.," *Radiology*, vol. 161, pp. 401–407, Nov. 1986.

[71] K. D. Merboldt, W. Hanicke, and J. Frahm, "Self-diffusion NMR imaging using stimulated echoes," *Journal of Magnetic Resonance*, vol. 64, pp. 479–486, Oct. 1985.

[72] J. Mattiello, P. J. Basser, and D. LeBihan, "Analytical Expressions for the b Matrix in NMR Diffusion Imaging and Spectroscopy," *Journal of Magnetic Resonance, Series A*, vol. 108, pp. 131–141, June 1994.

[73] Y. Zur, M. L. Wood, and L. J. Neuringer, "Spoiling of transverse magnetization in steady-state sequences," *Magnetic Resonance in Medicine*, vol. 21, pp. 251–263, Jan. 1991.

[74] C. Ganter, "Steady state of echo-shifted sequences with radiofrequency phase cycling.," *Magnetic Resonance in Medicine*, vol. 56, pp. 923–926, Oct. 2006.

[75] R. W. Brown, Y. C. N. Cheng, E. M. Haacke, M. R. Thompson, and R. Venkatesan, *Magnetic Resonance Imaging*. Physical Principles and Sequence Design, Chichester, UK: John Wiley & Sons, May 2014.

[76] K. Nicolay, A. V. D. Toorn, and R. M. Dijkhuizen, "In vivo diffusion spectroscopy. An overview," *NMR in Biomedicine*, vol. 8, pp. 365–374, Nov. 1995.

[77] K. Nicolay, K. P. J. Braun, R. A. d. Graaf, R. M. Dijkhuizen, and M. J. Kruiskamp, "Diffusion NMR spectroscopy," *NMR in Biomedicine*, vol. 14, pp. 94–111, Apr. 2001.

[78] E. O. Stejskal and J. E. Tanner, "Spin Diffusion Measurements: Spin Echoes in the Presence of a Time-Dependent Field Gradient," *The Journal of Chemical Physics*, vol. 42, pp. 288–292, Jan. 1965.

[79] J. E. Tanner, "Use of the stimulated echo in NMR diffusion studies," *The Journal of Chemical Physics*, vol. 52, p. 2523, 1970.

[80] A. Haase, J. Frahm, W. Hanicke, and D. Matthaei, "1H NMR chemical shift selective (CHESS) imaging," *Physics in Medicine and Biology*, vol. 30, no. 4, pp. 341–344, 1985.

[81] R. J. Ogg, R. B. Kingsley, and J. S. Taylor, "WET, a T1- and B1-Insensitive Water-Suppression Method for in Vivo Localized 1H NMR Spectroscopy," *Journal of Magnetic Resonance. Series B*, vol. 104, pp. 1–10, May 1994.

[82] I. Tkáč, Z. Starcuk, I. Y. Choi, and R. Gruetter, "In vivo 1H NMR spectroscopy of rat brain at 1 ms echo time.," *Magnetic Resonance in Medicine*, vol. 41, pp. 649–656, Apr. 1999.

[83] Q. Ye, C. F. Danzer, A. Fuchs, C. Wolfrum, and M. Rudin, "Hepatic lipid composition differs between ob/ob and ob/+ control mice as determined by using in vivo localized proton magnetic resonance spectroscopy," *Magnetic Resonance Materials in Physics, Biology and Medicine*, vol. 25, pp. 381–389, Oct. 2012.

[84] J. Lundbom, A. Hakkarainen, B. Fielding, S. Söderlund, J. Westerbacka, M. R. Taskinen, and N. Lundbom, "Characterizing human adipose tissue lipids by long echo time 1H-MRS in vivo at 1.5 Tesla: validation by gas chromatography.," *NMR in Biomedicine*, vol. 23, pp. 466–472, June 2010.

[85] J. Ren, A. D. Sherry, and C. R. Malloy, "$^{1}$H MRS of intramyocellular lipids in soleus muscle at 7 T: Spectral simplification by using long echo times without water suppression," *Magnetic Resonance in Medicine*, vol. 64, pp. 662–671, Sept. 2010.

[86] G. Hamilton, M. S. Middleton, M. Bydder, T. Yokoo, J. B. Schwimmer, Y. Kono, H. M. Patton, J. E. Lavine, and C. B. Sirlin, "Effect of PRESS and STEAM sequences on magnetic resonance spectroscopic liver fat quantification.," *Journal of Magnetic Resonance Imaging*, vol. 30, pp. 145–152, July 2009.

[87] A. Yahya and B. G. Fallone, "T(2) determination of the J-coupled methyl protons of lipids: In vivo ilustration with tibial bone marrow at 3 T.," *Journal of Magnetic Resonance Imaging*, vol. 31, pp. 1514–1521, June 2010.

[88] A. Yahya, A. G. Tessier, and B. G. Fallone, "Effect of J-coupling on lipid composition determination with localized proton magnetic resonance spectroscopy at 9.4 T," *Journal of Magnetic Resonance Imaging*, vol. 34, pp. 1388–1396, Dec. 2011.

[89] D. Y. Breitkreutz, B. G. Fallone, and A. Yahya, "Effect of J coupling on 1.3-ppm lipid methylene signal acquired with localised proton MRS at 3T," *NMR in Biomedicine*, vol. 28, pp. 1324–1331, Oct. 2015.

[90] J. Lundbom, S. Heikkinen, B. Fielding, A. Hakkarainen, M. R. Taskinen, and N. Lundbom, "PRESS echo time behavior of triglyceride resonances at 1.5 T: Detecting $\omega$-3 fatty acids in adipose tissue in vivo," *Journal of Magnetic Resonance*, vol. 201, pp. 39–47, Nov. 2009.

[91] A. Troitskaia, B. G. Fallone, and A. Yahya, "Long echo time proton magnetic resonance spectroscopy for estimating relative measures of lipid unsaturation at 3 T," *Journal of Magnetic Resonance Imaging*, vol. 37, pp. 944–949, Apr. 2013.

[92] A. Bingölbali, B. G. Fallone, and A. Yahya, "Comparison of optimized long echo time STEAM and PRESS proton MR spectroscopy of lipid olefinic protons at 3 Tesla.," *Journal of Magnetic Resonance Imaging*, vol. 41, pp. 481–486, Feb. 2015.

[93] M. I. Altbach, M. A. Mattingly, M. F. Brown, and A. F. Gmitro, "Magnetic Resonance Imaging of Lipid Deposits in Human Atheroma via a Stimulated-Echo Diffusion-Weighted Technique," *Magnetic Resonance in Medicine*, vol. 20, pp. 319–326, Jan. 1991.

[94] A. Lehnert, J. Machann, G. Helms, C. D. Claussen, and F. Schick, "Diffusion characteristics of large molecules assessed by proton MRS on a whole-body MR system.," *Magnetic Resonance Imaging*, vol. 22, pp. 39–46, Jan. 2004.

[95] L. Xiao and E. X. Wu, "Diffusion-weighted magnetic resonance spectroscopy: a novel approach to investigate intramyocellular lipids.," *Magnetic Resonance in Medicine*, vol. 66, pp. 937–944, Oct. 2011.

[96] V. Brandejsky, R. Kreis, and C. Boesch, "Restricted or severely hindered diffusion of intramyocellular lipids in human skeletal muscle shown by in vivo proton MR spectroscopy.," *Magnetic Resonance in Medicine*, vol. 67, pp. 310–316, Feb. 2012.

[97] A. M. Wang, P. Cao, A. Yee, D. Chan, and E. X. Wu, "Detection of extracellular matrix degradation in intervertebral disc degeneration by diffusion magnetic resonance spectroscopy," *Magnetic Resonance in Medicine*, vol. 73, pp. 1703–1712, May 2014.

[98] M. A. Thomas, H. K. Chung, and H. Middlekauff, "Localized two-dimensional$^1$H magnetic resonance exchange spectroscopy: A preliminary evaluation in human muscle," *Magnetic Resonance in Medicine*, vol. 53, pp. 495–502, Mar. 2005.

[99] S. S. Velan, C. Durst, S. K. Lemieux, R. R. Raylman, R. Sridhar, R. G. Spencer, G. R. Hobbs, and M. A. Thomas, "Investigation of muscle lipid metabolism by localized one- and two-dimensional MRS techniques using a clinical 3T MRI/MRS scanner.," *Journal of Magnetic Resonance Imaging*, vol. 25, pp. 192–199, Jan. 2007.

[100] S. S. Velan, N. Said, C. Durst, S. Frisbee, J. Frisbee, R. R. Raylman, M. A. Thomas, V. M. Rajendran, R. G. Spencer, and S. E. Alway, "Distinct patterns of fat metabolism in skeletal muscle of normal-weight, overweight, and obese humans.," *American Journal of Physiology - Regulatory, Integrative and Comparative Physiology*, vol. 295, pp. R1060–5, Oct. 2008.

[101] D. G. Carey, A. B. Jenkins, L. V. Campbell, J. Freund, and D. J. Chisholm, "Abdominal Fat and Insulin Resistance in Normal and Overweight Women: Direct Measurements Reveal a Strong Relationship in Subjects at Both Low and High Risk of NIDDM," *Diabetes*, vol. 45, pp. 633–638, May 1996.

[102] M. Manco, A. V. Greco, E. Capristo, D. Gniuli, A. De Gaetano, and G. Gasbarrini, "Insulin resistance directly correlates with increased saturated fatty acids in skeletal muscle triglycerides," *Metabolism*, vol. 49, pp. 220–224, Feb. 2000.

[103] M. Bydder, O. Girard, G. Hamilton, and G. Hamilton, "Mapping the double bonds in triglycerides.," *Magnetic Resonance Imaging*, vol. 29, pp. 1041–1046, Oct. 2011.

[104] B. Leporq, S. A. Lambert, M. Ronot, V. Vilgrain, and B. E. Van Beers, "Quantification of the triglyceride fatty acid composition with 3.0 T MRI," *NMR in Biomedicine*, vol. 27, pp. 1211–1221, Jan. 2014.

[105] G. H. Glover and E. Schneider, "Three-point dixon technique for true water/fat decomposition with B0 inhomogeneity correction," *Magnetic Resonance in Medicine*, vol. 18, pp. 371–383, Apr. 1991.

[106] D. Hernando, J. P. Haldar, B. P. Sutton, J. Ma, P. Kellman, and Z. P. Liang, "Joint estimation of water/fat images and field inhomogeneity map," *Magnetic Resonance in Medicine*, vol. 59, pp. 571–580, Mar. 2008.

[107] H. Yu, H. Yu, C. A. McKenzie, A. Shimakawa, A. Shimakawa, A. T. Vu, A. C. S. Brau, P. J. Beatty, A. R. Pineda, J. H. Brittain, J. H. Brittain, S. B. Reeder, and S. B. Reeder, "Multiecho reconstruction for simultaneous water-fat decomposition and T2* estimation.," *Journal of Magnetic Resonance Imaging*, vol. 26, pp. 1153–1161, Oct. 2007.

[108] M. Bydder, T. Yokoo, G. Hamilton, M. S. Middleton, A. D. Chavez, J. B. Schwimmer, J. E. Lavine, and C. B. Sirlin, "Relaxation effects in the quantification of fat using gradient echo imaging," *Magnetic Resonance Imaging*, vol. 26, no. 3, pp. 347–359, 2008.

[109] C.-Y. Liu, C. A. McKenzie, H. Yu, J. H. Brittain, and S. B. Reeder, "Fat quantification with IDEAL gradient echo imaging: Correction of bias from T1 and noise," *Magnetic Resonance in Medicine*, vol. 58, pp. 354–364, Aug. 2007.

[110] D. C. Karampinos, H. Yu, H. Yu, A. Shimakawa, A. Shimakawa, T. M. Link, and S. Majumdar, "T1-corrected fat quantification using chemical shift-based water/fat separation: application to skeletal muscle.," *Magnetic Resonance in Medicine*, vol. 66, pp. 1312–1326, Nov. 2011.

[111] H. Yu, A. Shimakawa, C. A. McKenzie, E. Brodsky, J. H. Brittain, and S. B. Reeder, "Multiecho water-fat separation and simultaneous R2* estimation with multifrequency fat spectrum modeling," *Magnetic Resonance in Medicine*, vol. 60, pp. 1122–1134, Nov. 2008.

[112] D. C. Karampinos, H. Yu, A. Shimakawa, T. M. Link, and S. Majumdar, "Chemical shift-based water/fat separation in the presence of susceptibility-induced fat resonance shift.," *Magnetic Resonance in Medicine*, vol. 68, pp. 1495–1505, Nov. 2012.

[113] W. Lu, H. Yu, A. Shimakawa, M. Alley, S. B. Reeder, and B. A. Hargreaves, "Water–fat separation with bipolar multiecho sequences," *Magnetic Resonance in Medicine*, vol. 60, pp. 198–209, July 2008.

[114] H. Yu, A. Shimakawa, C. A. McKenzie, W. Lu, S. B. Reeder, R. S. Hinks, and J. H. Brittain, "Phase and amplitude correction for multi-echo water-fat separation with bipolar acquisitions.," *Journal of Magnetic Resonance Imaging*, vol. 31, pp. 1264–1271, May 2010.

[115] H. Yu, A. Shimakawa, C. D. G. Hines, C. A. McKenzie, G. Hamilton, C. B. Sirlin, J. H. Brittain, and S. B. Reeder, "Combination of complex-based and magnitude-based multiecho water-fat separation for accurate quantification of fat-fraction.," *Magnetic Resonance in Medicine*, vol. 66, pp. 199–206, July 2011.

[116] D. Hernando, C. D. G. Hines, H. Yu, and S. B. Reeder, "Addressing phase errors in fat-water imaging using a mixed magnitude/complex fitting method," *Magnetic Resonance in Medicine*, vol. 67, pp. 638–644, Mar. 2012.

[117] P. Peterson and S. Mansson, "Fat quantification using multiecho sequences with bipolar gradients: investigation of accuracy and noise performance," *Magnetic Resonance in Medicine*, vol. 71, no. 1, pp. 219–229, 2014.

[118] D. C. Karampinos, T. Baum, L. Nardo, H. Alizai, H. Yu, J. Carballido-Gamio, S. P. Yap, A. Shimakawa, T. M. Link, and S. Majumdar, "Characterization of the regional distribution of skeletal muscle adipose tissue in type 2 diabetes using chemical shift-based water/fat separation.," *Journal of Magnetic Resonance Imaging*, vol. 35, pp. 899–907, Apr. 2012.

[119] D. G. Norris and J. M. S. Hutchison, "Concomitant magnetic field gradients and their effects on imaging at low magnetic field strengths," *Magnetic Resonance Imaging*, vol. 8, pp. 33–37, Jan. 1990.

[120] X. J. Zhou, Y. P. Du, M. A. Bernstein, H. G. Reynolds, J. K. Maier, and J. A. Polzin, "Concomitant magnetic-field-induced artifacts in axial echo planar imaging," *Magnetic Resonance in Medicine*, vol. 39, no. 4, pp. 596–605, 1998.

[121] Y. P. Du, X. Joe Zhou, and M. A. Bernstein, "Correction of concomitant magnetic field-induced image artifacts in nonaxial echo-planar imaging.," *Magnetic Resonance in Medicine*, vol. 48, pp. 509–515, Sept. 2002.

[122] K. F. King, A. Ganin, X. J. Zhou, and M. A. Bernstein, "Concomitant Gradient Field Effects in Spiral Scans," *Magnetic Resonance in Medicine*, vol. 41, pp. 103–112, Jan. 1999.

[123] T. J. Colgan, D. Hernando, S. D. Sharma, and S. B. Reeder, "The effects of concomitant gradients on chemical shift encoded MRI," *Magnetic Resonance in Medicine*, Sept. 2016.

[124] L. W. Hofstetter, G. Morrell, J. Kaggie, D. Kim, K. Carlston, and V. S. Lee, "T2* Measurement bias due to concomitant gradient fields.," *Magnetic Resonance in Medicine*, vol. 77, pp. 1562–1572, Apr. 2017.

[125] A. R. Pineda, S. B. Reeder, Z. Wen, and N. J. Pelc, "Cramér–Rao bounds for three-point decomposition of water and fat," *Magnetic Resonance in Medicine*, vol. 54, pp. 625–635, Sept. 2005.

[126] M. Tavassoli and W. H. Crosby, "Bone marrow histogenesis: a comparison of fatty and red marrow.," *Science (New York, N.Y.)*, vol. 169, pp. 291–293, July 1970.

[127] R. P. Custer, "Studies on the Structure and Function of Bone Marrow.," *The Journal of Laboratory and Clinical Medicine*, vol. 17, pp. 951–960, July 1932.

[128] R. P. Custer and F. E. Ahlfeldt, "Studies on the Structure and Function of Bone Marrow.," *The Journal of Laboratory and Clinical Medicine*, vol. 17, pp. 960–962, July 1932.

[129] M. E. Kricun, "Red-yellow marrow conversion: Its effect on the location of some solitary bone lesions," *Skeletal Radiology*, vol. 14, no. 1, pp. 10–19, 1985.

[130] P. S. Babyn, M. Ranson, and M. E. McCarville, "Normal bone marrow: signal characteristics and fatty conversion.," *Magnetic Resonance Imaging Clinics of North America*, vol. 6, pp. 473–495, Aug. 1998.

[131] E. L. Scheller, C. R. Doucette, B. S. Learman, W. P. Cawthorn, S. Khandaker, B. Schell, B. Wu, S.-Y. Ding, M. A. Bredella, P. K. Fazeli, B. Khoury, K. J. Jepsen, P. F. Pilch, A. Klibanski, C. J. Rosen, and O. A. MacDougald, "Region-specific variation in the properties of skeletal adipocytes reveals regulated and constitutive marrow adipose tissues," *Nature Communications*, vol. 6, p. 7808, 2015.

[132] M. Tavassoli, "Marrow adipose cells. Histochemical identification of labile and stable components.," *Archives of Pathology & Laboratory Medicine*, vol. 100, pp. 16–18, Jan. 1976.

[133] E. L. Scheller and C. J. Rosen, "What's the matter with MAT? Marrow adipose tissue, metabolism, and skeletal health.," *Annals of the New York Academy of Sciences*, vol. 1311, pp. 14–30, Apr. 2014.

[134] D. Schellinger, C. S. Lin, D. Fertikh, J. S. Lee, W. C. Lauerman, F. Henderson, and B. Davis, "Normal lumbar vertebrae: anatomic, age, and sex variance in subjects at proton MR spectroscopy–initial experience.," *Radiology*, vol. 215, pp. 910–916, June 2000.

[135] G. P. Liney, C. P. Bernard, D. J. Manton, L. W. Turnbull, and C. M. Langton, "Age, gender, and skeletal variation in bone marrow composition: a preliminary study at 3.0 Tesla.," *Journal of Magnetic Resonance Imaging*, vol. 26, pp. 787–793, Sept. 2007.

[136] E. Roldan-Valadez, C. Piña-Jimenez, R. Favila, and C. Rios, "Gender and age groups interactions in the quantification of bone marrow fat content in lumbar spine using 3T MR spectroscopy: A multivariate analysis of covariance (Mancova)," *European Radiology*, vol. 82, no. 11, pp. e697–e702, 2013.

[137] J. Martin, G. Nicholson, G. Cowin, C. Ilente, W. Wong, and D. Kennedy, "Rapid determination of vertebral fat fraction over a large range of vertebral bodies," *Journal of Medical Imaging and Radiation Oncology*, vol. 58, pp. 155–163, Apr. 2014.

[138] M. A. Bredella, S. M. Daley, M. K. Kalra, J. K. Brown, K. K. Miller, and M. Torriani, "Marrow Adipose Tissue Quantification of the Lumbar Spine by Using Dual-Energy CT and Single-Voxel (1)H MR Spectroscopy: A Feasibility Study.," *Radiology*, vol. 277, pp. 230–235, Oct. 2015.

[139] Q. M. Barber and A. Yahya, "Aspects of spinal bone marrow fat to water quantification with magnetic resonance spectroscopy at 3 T," *Biomedical Physics & Engineering Express*, vol. 1, p. 047001, Dec. 2015.

[140] J.-P. Kühn, D. Hernando, P. J. Meffert, S. Reeder, N. Hosten, R. Laqua, A. Steveling, S. Ender, H. Schröder, and D.-T. Pillich, "Proton-density fat fraction and simultaneous R2* estimation as an MRI tool for assessment of osteoporosis.," *European Radiology*, vol. 23, pp. 3432–3439, Dec. 2013.

[141] T. Baum, S. P. Yap, M. Dieckmeyer, S. Ruschke, H. Eggers, H. Kooijman, E. J. Rummeny, J. S. Bauer, and D. C. Karampinos, "Assessment of whole spine vertebral bone marrow fat using chemical shift-encoding based water-fat MRI," *Journal of Magnetic Resonance Imaging*, vol. 42, pp. 1018–1023, Oct. 2015.

[142] D. C. Karampinos, S. Ruschke, M. Dieckmeyer, H. Eggers, H. Kooijman, E. J. Rummeny, J. S. Bauer, and T. Baum, "Modeling of T2* decay in vertebral bone marrow fat quantification," *NMR in Biomedicine*, vol. 28, no. 11, pp. 1535–1542, 2015.

[143] J. C. Pichardo, R. J. Milner, and W. E. Bolch, "MRI measurement of bone marrow cellularity for radiation dosimetry.," *Journal of Nnuclear Medicine*, vol. 52, pp. 1482–1489, Sept. 2011.

[144] I. J. MacEwan, N. E. Glembotski, D. D'Lima, W. Bae, K. Masuda, H. H. Rashidi, L. K. Mell, and M. Bydder, "Proton density water fraction as a biomarker of bone marrow cellularity: validation in ex vivo spine specimens.," *Magnetic Resonance Imaging*, vol. 32, pp. 1097–1101, Nov. 2014.

[145] L. Arentsen, M. Yagi, Y. Takahashi, P. J. Bolan, M. White, D. Yee, and S. Hui, "Validation of marrow fat assessment using noninvasive imaging with histologic examination of human bone samples.," *Bone*, vol. 72, pp. 118–122, Mar. 2015.

[146] C. J. Rosen, C. Ackert-Bicknell, J. P. Rodriguez, and A. M. Pino, "Marrow fat and the bone microenvironment: developmental, functional, and pathological implications.," *Critical Reviews in Eukaryotic Gene Expression*, vol. 19, no. 2, pp. 109–124, 2009.

[147] H. Kugel, C. Jung, O. Schulte, and W. Heindel, "Age- and sex-specific differences in the 1H-spectrum of vertebral bone marrow.," *Journal of Magnetic Resonance Imaging*, vol. 13, pp. 263–268, Feb. 2001.

[148] J. F. Griffith, D. K. W. Yeung, H. T. Ma, J. C. S. Leung, T. C. Y. Kwok, and P. C. Leung, "Bone marrow fat content in the elderly: A reversal of sex difference seen in younger subjects," *Journal of Magnetic Resonance Imaging*, vol. 36, pp. 225–230, July 2012.

[149] H. Ishijima, H. Ishizaka, H. Horikoshi, and M. Sakurai, "Water fraction of lumbar vertebral bone marrow estimated from chemical shift misregistration on MR imaging: normal variations with age and sex.," *American Journal of Roentgenology*, vol. 167, pp. 355–358, Aug. 1996.

[150] B. A. Gower, T. R. Nagy, M. I. Goran, and M. J. Toth, "Fat distribution and plasma lipid-lipoprotein concentrations in pre-and postmenopausal women," *International Journal of Obesity*, vol. 22, no. 7, pp. 605–611, 1998.

[151] M. J. Toth, A. Tchernof, C. K. Sites, and E. T. Poehlman, "Menopause-related changes in body fat distribution.," *Annals of the New York Academy of Sciences*, vol. 904, pp. 502–506, May 2000.

[152] K. Blouin, A. Boivin, and A. Tchernof, "Androgens and body fat distribution.," *The Journal of Steroid Biochemistry and Molecular Biology*, vol. 108, pp. 272–280, Feb. 2008.

[153] H. S. Walker, R. B. Dietrich, B. D. Flannigan, R. B. Lufkin, W. J. Peacock, and H. Kangarloo, "Magnetic resonance imaging of the pediatric spine.," *Radiographics*, vol. 7, pp. 1129–1152, Nov. 1987.

[154] G. H. Sebag, J. Dubois, M. Tabet, A. Bonato, and D. Lallemand, "Pediatric spinal bone marrow: assessment of normal age-related changes in the MRI appearance.," *Pediatric Radiology*, vol. 23, no. 7, pp. 515–518, 1993.

[155] A. Taccone, M. Oddone, M. Occhi, A. Dell'Acqua, and M. A. Ciccone, "MRI "road-map" of normal age-related bone marrow," *Pediatric Radiology*, vol. 25, no. 8, pp. 588–595, 1995.

[156] K. Foster, S. Chapman, and K. Johnson, "MRI of the marrow in the paediatric skeleton.," *Clinical Radiology*, vol. 59, pp. 651–673, Aug. 2004.

[157] X. Li, D. Kuo, A. L. Schafer, A. Porzig, T. M. Link, D. Black, and A. V. Schwartz, "Quantification of vertebral bone marrow fat content using 3 tesla MR spectroscopy: Reproducibility, vertebral variation, and applications in osteoporosis," *Journal of Magnetic Resonance Imaging*, vol. 33, pp. 974–979, Mar. 2011.

[158] J. Lundbom, A. Hakkarainen, S. Söderlund, J. Westerbacka, N. Lundbom, and M. R. Taskinen, "Long-TE 1H MRS suggests that liver fat is more saturated than subcutaneous and visceral fat.," *NMR in Biomedicine*, vol. 24, pp. 238–245, Apr. 2011.

[159] J. Walecki, M. J. Michalak, E. Michalak, and Z. T. Bilinska, "Usefulness of 1 H MR spectroscopy in the evaluation of myocardial metabolism in patients with dilated idiopathic cardiomyopathy: pilot study1," *Academic Radiology*, 2003.

[160] S. Hammer, A. P. J. de Vries, P. de Heer, M. B. Bizino, R. Wolterbeek, T. J. Rabelink, J. Doornbos, and H. J. Lamb, "Metabolic Imaging of Human Kidney Triglyceride Content: Reproducibility of Proton Magnetic Resonance Spectroscopy," *PLOS ONE*, vol. 8, p. e62209, Apr. 2013.

[161] I. A. Bobulescu, Y. Lotan, J. Zhang, T. R. Rosenthal, J. T. Rogers, B. Adams-Huet, K. Sakhaee, and O. W. Moe, "Triglycerides in the Human Kidney Cortex: Relationship with Body Size," *PLOS ONE*, vol. 9, p. e101285, Aug. 2014.

[162] L. S. Szczepaniak, P. Nurenberg, D. Leonard, J. D. Browning, J. S. Reingold, S. Grundy, H. H. Hobbs, and R. L. Dobbins, "Magnetic resonance spectroscopy to measure hepatic triglyceride content: Prevalence of hepatic steatosis in the general population," *American Journal of Physiology - Endocrinology and Metabolism*, vol. 288, pp. E462–E468, Feb. 2005.

[163] D. C. Karampinos, S. Ruschke, O. Gordijenko, E. Grande Garcia, H. Kooijman, R. Burgkart, E. J. Rummeny, J. S. Bauer, and T. Baum, "Association of MRS-based vertebral bone marrow fat fraction with bone strength in a human in vitro model," *Journal of Osteoporosis*, vol. 2015, pp. 1–8, Jan. 2015.

[164] M. A. Bredella, M. Torriani, R. H. Ghomi, B. J. Thomas, D. J. Brick, A. V. Gerweck, C. J. Rosen, A. Klibanski, and K. K. Miller, "Vertebral bone marrow fat is positively associated with visceral fat and inversely associated with IGF-1 in obese women," *Obesity*, vol. 19, pp. 49–53, Jan. 2011.

[165] L. Ollivier, H. Brisse, and J. Leclère, "Bone marrow imaging: Follow-up after treatment in cancer patients," *Cancer Imaging*, vol. 2, pp. 90–92, Dec. 2002.

[166] H. E. Daldrup-Link, T. Henning, and T. M. Link, "MR imaging of therapy-induced changes of bone marrow.," *European Radiology*, vol. 17, pp. 743–761, Mar. 2007.

[167] P. J. Bolan, L. Arentsen, T. Sueblinvong, Y. Zhang, S. Moeller, J. S. Carter, L. S. Downs, R. Ghebre, D. Yee, J. Froelich, and S. Hui, "Water-fat MRI for assessing changes in bone marrow composition due to radiation and chemotherapy in gynecologic cancer patients.," *Journal of Magnetic Resonance Imaging*, vol. 38, pp. 1578–1584, Dec. 2013.

[168] R. Carmona, J. Pritz, M. Bydder, S. Gulaya, H. Zhu, C. W. Williamson, C. S. Welch, F. Vaida, G. Bydder, and L. K. Mell, "Fat composition changes in bone marrow during chemotherapy and radiation therapy," *International Journal of Radiation Oncology, Biology, Physics*, vol. 90, pp. 155–163, Sept. 2014.

[169] M. Cristy, "Active bone marrow distribution as a function of age in humans," *Physics in Medicine and Biology*, vol. 26, pp. 389–400, May 1981.

[170] L. A. Moulopoulos and M. A. Dimopoulos, "Magnetic resonance imaging of the bone marrow in hematologic malignancies," *Blood*, vol. 90, no. 6, pp. 2127–2147, 1997.

[171] D. J. Weidlich, A. Hock, S. Ruschke, D. Franz, K. Steiger, T. Skurk, H. Hauner, E. J. Rummeny, and D. C. Karampinos, "Probing bone marrow adipocyte cell size in vivo at a clinical 3 T scanner using high b-value DW-MRS at long diffusion times," in *Proceedings of the 25th Scientific Meeting of ISMRM*, (Honolulu, Hawaii (USA)), p. 1227, 2017.